Received: 6 May 2026 | Revised: 27 July 2026 | Accepted: 18 September 2026

DOI: 10.33012/navi.793

ORIGINAL ARTICLE

Orbit Uncertainty Covariance Adaptation for LEO Phase and Doppler Differential Positioning

Yangkang Yu* | **Ahmed El-Mowafy** | **Amir Allahvirdi-Zadeh**

[1] School of Earth and Planetary Sciences, Curtin University, Perth, WA, Australia

Correspondence
*Corresponding author: Yangkang Yu
School of Earth and Planetary Sciences, Curtin University, GPO Box U 1987, Perth, WA 6845, Australia.
Email: yangkang.yu@outlook.com

Abstract

Navigating with opportunistic signals from low-Earth-orbit satellites is a promising alternative to traditional systems, yet it remains hindered by the large uncertainty of publicly accessible orbit products. Kilometer-level ephemeris errors project into the measurement domain as systematic, time-varying biases, often causing standard filters to fail because they rely too heavily on contaminated carrier-phase or Doppler observations. This paper introduces orbit uncertainty covariance adaptation (OUCA), a stochastic framework that maps orbit uncertainty directly into the observation space. By modeling satellite position and velocity uncertainty in the orbital frame and projecting it through the time-varying observation geometry, OUCA provides a physically consistent way to adapt measurement weighting in real time while preserving same-epoch coupling between phase and Doppler observations. The results show two primary findings. First, OUCA is effective for all three observation modes, namely, phase-only, Doppler-only, and phase+Doppler. A representative two-line-element (TLE) scenario with a 10-km baseline shows how the gains differ across the three modes: OUCA reduces the final three-dimensional error from 102.617 m to 10.102 m for the phase-only mode (90.2%), from 17.725 m to 6.253 m for the Doppler-only mode (64.7%), and from 56.232 m to 4.581 m for the phase+Doppler mode (91.9%). Second, once OUCA is applied, the phase+Doppler mode provides an effective joint solution across different orbit-quality conditions. Under high-precision orbit conditions, this mode retains the same centimeter-level positioning accuracy as the phase-only mode. Under TLE-grade orbit conditions, the phase+Doppler mode improves positioning accuracy compared with the Doppler-only mode.

Keywords

ambiguity resolution, covariance adaptation, differential positioning, ephemeris uncertainty, LEO PNT, opportunistic navigation, phase+Doppler processing

1 | INTRODUCTION

The global field of positioning, navigation, and timing (PNT) is undergoing a major change, driven by the growth of low-Earth-orbit (LEO) megaconstellations (P. Liu et al., 2025). With tens of thousands of satellites planned for deployment

Licensed under CC-BY 4.0 © 2026 Institute of Navigation

by SpaceX, OneWeb, and Amazon, the high density and close distance of these platforms offer a strong alternative to traditional medium-Earth-orbit (MEO) systems (Del Portillo et al., 2019). The dense spatial distribution and stronger received signal power of LEO satellites can improve signal availability in challenging environments such as urban canyons and dense foliage (Humphreys et al., 2023; P. Liu et al., 2025). Moreover, the high angular velocity of LEO satellites leads to fast geometry changes, allowing navigation filters to converge in a fraction of the time required by MEO constellations (Iannucci & Humphreys, 2024; Khalife & Kassas, 2023).

Much research has focused on studying the signal structures of broadband LEO downlinks (Garcia et al., 2024; Humphreys et al., 2023) and developing specialized hardware and processing chains for high-fidelity signal acquisition (Diouf et al., 2021; Farhangian & Landry, 2020). These earlier studies have enabled numerous positioning techniques, ranging from time difference of arrival and frequency difference of arrival (Elgamoudi et al., 2020; Gholami et al., 2013) to advanced carrier tracking in multipath-rich channels (Dun et al., 2020; Kazaz et al., 2022). To date, opportunistic LEO work has developed along two primary observable choices. Doppler measurements, which exploit the large frequency shifts caused by LEO dynamics, have been applied to both static and kinematic positioning in non-differential and differential forms (Allahvirdi-Zadeh et al., 2025; Baron et al., 2024; Psiaki, 2021; Shi et al., 2023; Zhao et al., 2023). Carrier phase, which aims for high precision through ambiguity resolution, has been primarily used in differential form (Khalife & Kassas, 2023; Khalife et al., 2020, 2022).

Despite this progress, opportunistic LEO navigation is still limited by the uncertainty of satellite ephemeris. Unlike global navigation satellite system (GNSS) satellites, which broadcast high-precision orbital parameters, broadband LEO operators usually do not provide public users with orbit products of comparable quality (Kozhaya et al., 2025; Q. Li et al., 2023). In practice, the available orbit source may range from precise externally generated products to degraded broadcast solutions and, in the worst case, public two-line elements (TLEs). When propagated with the simplified general perturbations 4 (SGP4) model, TLE-based orbits can contain errors of several kilometers (Levit & Marshall, 2011; Vallado et al., 2006). Differential processing, including carrier-phase differential LEO methods (Khalife & Kassas, 2023) and differential Doppler workflows (Jiang et al., 2021; Zhao et al., 2023), removes satellite clock terms and reduces much of the common atmospheric delay, but it cannot eliminate the baseline-dependent effect of orbit error. Broader analyses of orbital and tracking error propagation in LEO constellations likewise show that once public TLE/SGP4 products are used, orbit error can no longer be treated as a small secondary disturbance (El-Mowafy et al., 2023; Khairallah & Kassas, 2024). For carrier phase, this error grows quickly with baseline length, appears as a time-varying slope that disturbs ambiguity estimation, and can drive standard real-time kinematic filters to divergence (Khalife & Kassas, 2023). Doppler alone usually cannot provide the centimeter-level precision targeted by high-accuracy applications unless clean Doppler measurements are available and are coupled with dedicated network-based precise orbit determination infrastructure (Allahvirdi-Zadeh et al., 2026). Residual orbit error in differential Doppler positioning also grows rapidly with baseline length and quickly reduces positioning consistency (Zhao et al., 2023). Therefore, the central difficulty is not only that orbit products are imperfect, but that the same orbit error affects phase and Doppler in very different ways.

This difference becomes most important when phase and Doppler are used together. In principle, joint processing should combine the precision of carrier phase with the robustness of Doppler over a wide range of orbit quality. In practice,

traditional extended Kalman filter (EKF) architectures do not explicitly account for orbit uncertainty. They assign weights according to nominal thermal noise, typically on the order of millimeters for carrier phase and centimeters per second for Doppler, while ignoring the much larger orbit-induced uncertainty. As the ephemeris degrades, this weighting creates an overconfidence bias. The filter is then pulled toward orbit-contaminated phase measurements, and the more reliable Doppler information can no longer fulfill its intended stabilizing role (Elgamoudi et al., 2020; Leng et al., 2014; X. Li et al., 2019). Robust and adaptive filtering methods have long been used in geodetic and navigation estimation to handle contaminated observations (Pan et al., 2021; Y. Yang et al., 2001). However, these general methods do not explicitly model how uncertain LEO orbit products propagate through time-varying geometry into the coupled carrier-phase and Doppler observation domain considered here. Some studies have attempted to address this issue by expanding the state vector with explicit orbit parameters (Khairallah & Kassas, 2024; Leng et al., 2016), but such methods often face weak observability or rapid state growth once many LEO satellites are tracked at the same time. Instead, what is needed is a way to represent orbit uncertainty directly in the observation model, such that the balance between phase and Doppler can change with the actual orbit quality.

In this paper, we address this problem with orbit uncertainty covariance adaptation (OUCA). OUCA maps externally provided or prior orbit error covariance directly into the observation covariance. Satellite position and velocity uncertainty are first described in the radial, transverse, and normal (RTN) frame and then projected through the time-varying geometry into the Earth-centered, Earth-fixed (ECEF) frame and the differential measurement domain. In this way, the filter can reduce the weight of observables that are most strongly affected by orbit error at each epoch. LEO orbit error may remain strongly correlated in the RTN frame, but its effect in the observation domain evolves rapidly, which helps explain why covariance adaptation remains effective even under time-correlated orbit errors. The same framework propagates the shared orbit error into the joint phase and Doppler covariance. Through Monte Carlo simulations under decimeter-grade, meter-grade, and TLE-grade orbit conditions with grade-dependent RTN Gaussian orbit uncertainty, we show that OUCA is effective for all three observation modes, namely, phase-only, Doppler-only, and phase+Doppler. Once OUCA is applied, the phase+Doppler mode provides an effective joint solution across these orbit-quality conditions. Under high-precision orbit conditions, this mode retains centimeter-level positioning accuracy and improves ambiguity-fixing performance compared with the phase-only mode. Under TLE-grade orbit conditions, the phase+Doppler mode improves positioning accuracy compared with the Doppler-only mode.

The remainder of this paper is organized as follows. Section 2 establishes the joint differential measurement models. Section 3 presents the OUCA stochastic modeling framework. Section 4 describes the simulation setup and evaluates the framework across orbit quality, observation mode, and differencing architecture, including the ambiguity resolution. Section 5 concludes the paper.

2 | MEASUREMENT MODELS FOR DIFFERENTIAL CARRIER-PHASE AND DOPPLER JOINT POSITIONING

This section introduces the carrier-phase and Doppler observation models used throughout the paper. We begin with the undifferenced observables, then derive

the single-difference (SD) and double-difference (DD) forms, and finally define the nominal covariance matrices that are later augmented by OUCA in Section 3.

2.1 | Undifferenced Carrier-Phase and Doppler Models

Following the carrier-phase differential LEO formulation reported by Khalife and Kassas (2023), the undifferenced carrier-phase observable φ_r^s is modeled as follows:

$$\varphi_r^s = \rho_r^s + c\left(\delta t_r - \delta t^s\right) + T_r^s - I_r^s + \lambda N_r^s + \varepsilon_r^s \tag{1}$$

where δt_r and δt^s are clock biases, T_r^s and I_r^s are the tropospheric and ionospheric delays, N_r^s is the unknown integer ambiguity, and ε_r^s represents the phase measurement noise.

Carrier Doppler observation models for LEO navigation have been developed by Allahvirdi-Zadeh et al. (2025), Baron et al. (2024), and Psiaki (2021). The measured carrier Doppler shift in hertz is converted into the equivalent pseudorange rate in meters per second using the carrier frequency and the speed of light (Psiaki, 2021; Baron et al., 2024). The resulting observable is modeled using the following simplified pseudorange rate form (Shi et al., 2023; Zhao et al., 2023):

$$d_r^s = \dot{\rho}_r^s + c\left(\dot{\delta} t_r - \dot{\delta} t^s\right) + \dot{T}_r^s - \dot{I}_r^s + e_r^s \tag{2}$$

Here, d_r^s denotes the pseudorange rate. $\dot{\delta} t_r$ and $\dot{\delta} t^s$ represent the receiver and satellite clock drifts, whereas $\dot{T}_r^s$ and $\dot{I}_r^s$ denote the tropospheric and ionospheric delay rates, respectively. The term e_r^s includes measurement noise and, more importantly, the residual orbit error, which has strong spatial and temporal correlations. The geometric range is $\rho_r^s = \| \boldsymbol{p}^s - \boldsymbol{p}_r \|$, and the corresponding range rate is as follows:

$$\dot{\rho}_r^s = \frac{\left(\boldsymbol{p}^s - \boldsymbol{p}_r\right)^{\mathrm{T}}}{\rho_r^s}\left(\boldsymbol{v}^s - \boldsymbol{v}_r\right) \tag{3}$$

Here and in the following, vector quantities are denoted in boldface. $\boldsymbol{p}_r$ and $\boldsymbol{v}_r$ denote the position and velocity of receiver r, respectively, whereas $\boldsymbol{p}^s$ and $\boldsymbol{v}^s$ denote the position and velocity of satellite s at the transmission time. If the receiver is static, then $\boldsymbol{v}_r = \boldsymbol{0}$. Hereafter, the term "Doppler" refers to this pseudorange rate observable.

For simplicity, receiver and satellite hardware biases are not written explicitly in the phase and Doppler observation equations. For the phase observable, these biases are constant over a pass and are absorbed into the ambiguity and clock terms, whereas for the Doppler observable, they differentiate to zero. Compared with Doppler, carrier phase offers much higher precision but is also more sensitive to orbit-induced line-of-sight mismatch, because the residual projects directly into the ambiguity-contaminated phase domain.

For subsequent covariance propagation, the undifferenced (UD) noise terms are stacked as follows:

$$\boldsymbol{\varepsilon}_{\mathrm{UD}} = \begin{bmatrix} \boldsymbol{\varepsilon}_r^{\mathrm{T}} & \boldsymbol{\varepsilon}_b^{\mathrm{T}} \end{bmatrix}^{\mathrm{T}}, \qquad \boldsymbol{e}_{\mathrm{UD}} = \begin{bmatrix} \boldsymbol{e}_r^{\mathrm{T}} & \boldsymbol{e}_b^{\mathrm{T}} \end{bmatrix}^{\mathrm{T}} \tag{4}$$

with the nominal undifferenced covariance matrices:

$$\Sigma_{\varphi\varphi,\mathrm{nom,UD}} = \mathrm{diag}\left(\sigma^2_{\varphi,r,s_0}, \sigma^2_{\varphi,r,s_1}, \ldots, \sigma^2_{\varphi,r,s_m}, \sigma^2_{\varphi,b,s_0}, \sigma^2_{\varphi,b,s_1}, \ldots, \sigma^2_{\varphi,b,s_m}\right) \tag{5}$$

$$\Sigma_{dd,\mathrm{nom,UD}} = \mathrm{diag}\left(\sigma^2_{d,r,s_0}, \sigma^2_{d,r,s_1}, \ldots, \sigma^2_{d,r,s_m}, \sigma^2_{d,b,s_0}, \sigma^2_{d,b,s_1}, \ldots, \sigma^2_{d,b,s_m}\right) \tag{6}$$

$$\Sigma_{\varphi d,\mathrm{nom,UD}} = \Sigma^{1/2}_{\varphi\varphi,\ \mathrm{nom,UD}} \mathbf{R}_{\varphi d,\mathrm{UD}} \Sigma^{1/2}_{dd,\ \mathrm{nom,UD}} \tag{7}$$

The receiver subscripts b and r denote the base and rover, respectively. The matrix $\mathbf{R}_{\varphi d,\mathrm{UD}}$ denotes the nominal phase Doppler random noise correlation matrix. Typically, $\mathbf{R}_{\varphi d,\mathrm{UD}} = \rho_{\varphi d}\mathbf{I}_{2m+2}$, where $\rho_{\varphi d} \in [-1, 1]$ denotes the correlation coefficient between the Doppler and phase random noise components. Because $\Sigma_{\varphi\varphi,\mathrm{nom,UD}}$ and $\Sigma_{dd,\ \mathrm{nom,UD}}$ are diagonal here, their square roots are taken elementwise on the diagonal. The corresponding nominal undifferenced joint covariance is as follows:

$$\Sigma_{\mathrm{nom,UD}} = \begin{bmatrix} \Sigma_{\varphi\varphi,\mathrm{nom,UD}} & \Sigma_{\varphi d,\mathrm{nom,UD}} \\ \Sigma^{\mathrm{T}}_{\varphi d,\mathrm{nom,UD}} & \Sigma_{dd,\mathrm{nom,UD}} \end{bmatrix} \tag{8}$$

These terms provide the baseline stochastic model that is propagated to the SD and DD levels before the orbit-induced covariance increment is added.

2.2 | SD Carrier-Phase and Doppler Model

Differential processing is adopted to suppress satellite clock terms, reduce common propagation mismatch, and transform the estimation target from an absolute position solution to a relative baseline solution. Following the work by Khalife and Kassas (2023) and Zhao et al. (2023), the base station and rover are assumed to use the same orbit source at a common receive epoch. The SD between receivers for satellite s is formed as $\Delta(\cdot)^s_r = (\cdot)^s_r - (\cdot)^s_b$:

$$\Delta\varphi^s_r = \Delta\rho^s_r + c\Delta\delta t_r + \Delta T^s_r - \Delta I^s_r + \lambda\Delta N^s_r + \Delta\varepsilon^s_r \tag{9}$$

$$\Delta d^s_r = \Delta\dot{\rho}^s_r + c\Delta\dot{\delta} t_r + \Delta\dot{T}^s_r - \Delta\dot{I}^s_r + \Delta e^s_r \tag{10}$$

where $\Delta\delta t_r = \delta t_r - \delta t_b$ and $\Delta\dot{\delta} t_r = \dot{\delta} t_r - \dot{\delta} t_b$ are the relative receiver clock bias and drift. Between-receiver differencing removes the satellite clock, much of the common atmospheric error, and the common component of the orbit-induced error. Because the rover and base line-of-sight vectors are close but not identical, a baseline-dependent orbit residual remains and increases with their angular separation. The satellite-dependent hardware bias is common to the two receivers and is removed by between-receiver differencing, whereas the remaining receiver-dependent bias is common to all satellites and is absorbed by the relative clock states.

Linearizing the SD carrier-phase and SD Doppler equations around the approximate rover position and velocity yields the following (Baron et al., 2024; Khalife & Kassas, 2023; Zhao et al., 2023):

$$y^s_{\varphi,\mathrm{SD}} = -\boldsymbol{u}^{s\ \mathrm{T}}_r \delta\boldsymbol{p} + c\Delta\delta t_r + \Delta T^s_r - \Delta I^s_r + \lambda\Delta N^s_r + \Delta\varepsilon^s_r \tag{11}$$

$$y^s_{d,\mathrm{SD}} = -\boldsymbol{g}^{s\,\mathrm{T}}_r \delta\boldsymbol{p} - \boldsymbol{u}^{s\,\mathrm{T}}_r \delta\boldsymbol{v} + c\Delta\dot{\delta}t_r + \Delta\dot{T}^s_r - \Delta\dot{I}^s_r + \Delta\dot{e}^s_r \tag{12}$$

where:

$$\boldsymbol{g}^s_r = \frac{\boldsymbol{v}^s - \boldsymbol{v}_r}{\rho^s_r} - \frac{\left(\boldsymbol{v}^s - \boldsymbol{v}_r\right)^{\mathrm{T}} \boldsymbol{\rho}^s_r}{\left(\rho^s_r\right)^3}\boldsymbol{\rho}^s_r, \quad \boldsymbol{u}^s_r = \frac{\boldsymbol{\rho}^s_r}{\rho^s_r}, \quad \boldsymbol{\rho}^s_r = \boldsymbol{p}^s - \boldsymbol{p}_r \tag{13}$$

Here, $\boldsymbol{u}^s_r$ is the rover-to-satellite unit line-of-sight vector, $\boldsymbol{g}^s_r$ is the Doppler position sensitivity, and $\delta\boldsymbol{v}$ denotes the rover velocity correction. Because the base station position and velocity are known, only the rover geometry contributes to the estimated position and velocity sensitivities. For a static receiver, $\delta\boldsymbol{v} = \mathbf{0}$. Stacking the innovations for the $m+1$ tracked satellites gives the following:

$$\boldsymbol{y}_{\mathrm{SD}} = \begin{bmatrix} \boldsymbol{y}^{\mathrm{T}}_{\varphi,\mathrm{SD}} & \boldsymbol{y}^{\mathrm{T}}_{d,\mathrm{SD}} \end{bmatrix}^{\mathrm{T}} = \mathbf{H}_{\mathrm{SD}}\boldsymbol{x}_{\mathrm{SD}} + \begin{bmatrix} \Delta\boldsymbol{\varepsilon}^{\mathrm{T}} & \Delta\boldsymbol{e}^{\mathrm{T}} \end{bmatrix}^{\mathrm{T}} \tag{14}$$

where $\mathbf{H}_{\mathrm{SD}}$ stacks the phase and Doppler sensitivity rows in Equations (11) and (12). The general SD state $\boldsymbol{x}_{\mathrm{SD}}$ contains the receiver position and velocity corrections, relative clock bias and drift, float ambiguities, and atmospheric nuisance terms. The lower-dimensional state used in the static experiments is specified in Section 4.1. With the undifferenced covariance matrices defined in Section 2.1, the SD transformation matrix is as follows:

$$\mathbf{S} = \begin{bmatrix} \mathbf{I}_{m+1} & -\mathbf{I}_{m+1} \end{bmatrix} \tag{15}$$

The joint SD covariance follows directly:

$$\Sigma_{\mathrm{nom,SD}} = \mathbf{S}_J \Sigma_{\mathrm{nom,UD}} \mathbf{S}^{\mathrm{T}}_J, \qquad \mathbf{S}_J = \mathrm{diag}(\mathbf{S}, \mathbf{S}) \tag{16}$$

This nominal covariance is the baseline stochastic model to which OUCA later adds the orbit-induced covariance.

2.3 | DD Carrier-Phase and Doppler Model

Subsequent differencing between satellite s and a reference satellite s_0 forms the DD, $\nabla\Delta(\cdot)^s_r = \Delta(\cdot)^s_r - \Delta(\cdot)^{s_0}_r$. This operation eliminates the relative receiver clock terms $\Delta\delta t_r$ and $\Delta\dot{\delta}t_r$, such that one ambiguity per nonreference satellite remains in the carrier-phase observables while the Doppler observables remain ambiguity-free:

$$\nabla\Delta\varphi^s_r = \nabla\Delta\rho^s_r + \lambda\nabla\Delta N^s_r + \nabla\Delta T^s_r - \nabla\Delta I^s_r + \nabla\Delta\varepsilon^s_r \tag{17}$$

$$\nabla\Delta d^s_r = \nabla\Delta\dot{\rho}^s_r + \nabla\Delta\dot{T}^s_r - \nabla\Delta\dot{I}^s_r + \nabla\Delta\dot{e}^s_r \tag{18}$$

The phase+Doppler estimator then combines the DD carrier-phase and DD Doppler observables within a common relative motion estimation framework. The carrier phase contributes high geometric precision, whereas the Doppler contributes ambiguity-free and dynamically robust information. Linearizing the DD

carrier-phase and DD Doppler equations around the approximate rover position and velocity yields the following (Khalife & Kassas, 2023; Zhao et al., 2023):

$$y^s_{\varphi,\mathrm{DD}} = -\left(\boldsymbol{u}^s - \boldsymbol{u}^{s_0}\right)^{\mathrm{T}} \delta\boldsymbol{p} + \lambda\nabla\Delta N^s_r + \nabla\Delta T^s_r - \nabla\Delta I^s_r + \nabla\Delta\varepsilon^s_r \tag{19}$$

$$y^s_{d,\mathrm{DD}} = -\left(\boldsymbol{g}^s_r - \boldsymbol{g}^{s_0}_r\right)^{\mathrm{T}} \delta\boldsymbol{p} - \left(\boldsymbol{u}^s - \boldsymbol{u}^{s_0}\right)^{\mathrm{T}} \delta\boldsymbol{v} + \nabla\Delta\dot{T}^s_r - \nabla\Delta\dot{I}^s_r + \nabla\Delta e^s_r \tag{20}$$

where:

$$\boldsymbol{g}^s_r = \frac{\boldsymbol{v}^s - \boldsymbol{v}_r}{\rho^s} - \frac{\left(\boldsymbol{v}^s - \boldsymbol{v}_r\right)^{\mathrm{T}} \boldsymbol{\rho}^s}{\left(\rho^s\right)^3}\boldsymbol{\rho}^s, \qquad \boldsymbol{u}^s = \frac{\boldsymbol{\rho}^s}{\rho^s}, \qquad \boldsymbol{\rho}^s = \boldsymbol{p}^s - \boldsymbol{p}_r \tag{21}$$

Here, $\boldsymbol{u}^s$ and $\boldsymbol{g}^s_r$ denote the rover-side line-of-sight vector and Doppler position sensitivity for satellite s, respectively. When the user receiver is static, the DD Doppler velocity correction term also vanishes because $\delta\boldsymbol{v} = \mathbf{0}$, while $\boldsymbol{g}^s_r$ remains the static receiver Doppler position sensitivity. Stacking the innovations of all non-reference satellites then yields the DD joint linear model:

$$\boldsymbol{y}_{\mathrm{DD}} = \begin{bmatrix} \boldsymbol{y}_{\varphi,\mathrm{DD}} \\ \boldsymbol{y}_{d,\mathrm{DD}} \end{bmatrix} = \begin{bmatrix} \mathbf{G}_{\varphi,\mathrm{DD}} & \mathbf{0} & \lambda\mathbf{I}_m & \mathbf{I}_m & -\mathbf{I}_m & \mathbf{0} & \mathbf{0} \\ \mathbf{G}_{d,p,\mathrm{DD}} & \mathbf{G}_{d,v,\mathrm{DD}} & \mathbf{0} & \mathbf{0} & \mathbf{0} & \mathbf{I}_m & -\mathbf{I}_m \end{bmatrix} \boldsymbol{x} + \begin{bmatrix} \nabla\Delta\boldsymbol{\varepsilon} \\ \nabla\Delta\boldsymbol{e} \end{bmatrix} \tag{22}$$

where $\boldsymbol{x}$ contains the position and velocity corrections, DD ambiguities, and DD atmospheric states. The matrices $\mathbf{G}_{\varphi,\mathrm{DD}}$, $\mathbf{G}_{d,p,\mathrm{DD}}$, and $\mathbf{G}_{d,v,\mathrm{DD}}$ collect the corresponding sensitivity rows. The nominal DD stochastic model is propagated from the SD model. If the SD innovations are ordered as $\{s_0, s_1, \ldots, s_m\}$, the DD transformation matrix is as follows:

$$\mathbf{D} = \begin{bmatrix} -1 & 1 & 0 & \cdots & 0 \\ -1 & 0 & 1 & \cdots & 0 \\ \vdots & \vdots & \vdots & \ddots & \vdots \\ -1 & 0 & 0 & \cdots & 1 \end{bmatrix} = \begin{bmatrix} -\mathbf{1}_m & \mathbf{I}_m \end{bmatrix} \tag{23}$$

Applying the same transformation to the phase and Doppler blocks gives the following:

$$\boldsymbol{\Sigma}_{\mathrm{nom,DD}} = \mathbf{D}_J \boldsymbol{\Sigma}_{\mathrm{nom,SD}} \mathbf{D}_J^{\mathrm{T}}, \qquad \mathbf{D}_J = \mathrm{diag}(\mathbf{D}, \mathbf{D}) \tag{24}$$

Equation (24) contains only nominal carrier-phase and Doppler noise. Residual orbit error introduces additional structured errors and same-epoch coupling that may exceed this nominal noise level.

3 | OUCA: OBSERVATION-DOMAIN COVARIANCE ADAPTATION OF EPHEMERIS UNCERTAINTY

This section derives OUCA as a propagation chain from orbit uncertainty to observation covariance. We first show how residual orbit error appears in differential

observations, then parameterize the error in the RTN frame, and map the error to ECEF position and velocity perturbations. These perturbations are subsequently propagated into the SD and DD covariance matrices used by the estimator.

3.1 | RTN Orbit Uncertainty and Its Observation-Domain Projection

To quantify the orbit-error effect in the most direct way, let $\delta \boldsymbol{p}^s_{\mathrm{ECEF}}(t) \in \mathbb{R}^3$ denote the residual orbit position error of satellite s expressed in the ECEF frame at epoch t. The resulting first-order range perturbation on the user–satellite link, obtained via a first-order Taylor-series expansion, is as follows (Khalife & Kassas, 2023; Zhao et al., 2023):

$$\Delta\rho^s_{\mathrm{orb}}(t) \approx (\boldsymbol{u}^s(t))^{\mathrm{T}} \delta \boldsymbol{p}^s_{\mathrm{ECEF}}(t) \tag{25}$$

where $\Delta\rho^s_{\mathrm{orb}}(t)$ is the first-order orbit-induced range perturbation for the link between the user and satellite s and $\boldsymbol{u}^s(t) \in \mathbb{R}^3$ denotes the user-to-satellite line-of-sight unit vector. In the SD covariance construction, the rover and base versions are written as $\boldsymbol{u}^s_r$ and $\boldsymbol{u}^s_b$. As the LEO satellite moves rapidly across the sky, this time-varying projection appears in the carrier phase as a slowly varying slope drift.

For the differential phase model, the between-receiver perturbation for satellite s becomes $\Delta\rho^s_{\mathrm{orb,SD}}(t) \approx (\boldsymbol{u}^s_b(t) - \boldsymbol{u}^s_r(t))^{\mathrm{T}} \delta \boldsymbol{p}^s_{\mathrm{ECEF}}(t)$. With the corresponding phase sensitivity defined as $\boldsymbol{a}^s(t) = \boldsymbol{u}^s_b(t) - \boldsymbol{u}^s_r(t) \in \mathbb{R}^3$, the induced variance is $\mathrm{Var}\left(\Delta\rho^s_{\mathrm{orb,SD}}\right) = \boldsymbol{a}^{s\,\mathrm{T}} \Sigma^s_p \boldsymbol{a}^s$, where $\Sigma^s_p \in \mathbb{R}^{3\times3}$ is the ECEF orbit position covariance of satellite s.

For short to medium baselines, the difference between rover and base viewing directions grows approximately linearly with the baseline length l, so $\|\boldsymbol{a}^s\| \propto l$. Consequently, the projected phase variance follows a scaling law:

$$\sigma^{s2}_{\varphi,\mathrm{orb}} \propto l^2 \tag{26}$$

Here, $\sigma^{s2}_{\varphi,\mathrm{orb}}$ denotes the orbit-induced phase variance contribution associated with satellite s, and the omitted proportionality factor depends on the orbit covariance magnitude and the instantaneous geometry. This quadratic scaling explains why long-baseline performance degrades rapidly as orbit quality worsens. Doppler is affected through the same geometry, but usually more weakly because it is primarily driven by velocity mismatch and by the time variation of the line-of-sight projection. The discussion above is given directly in the ECEF frame only to show the geometric effect; we now turn to a stochastic model for the underlying position and velocity errors.

The ECEF view above is useful for interpretation, but the stochastic model is more naturally defined in the RTN frame. Here, R, T, and N denote the radial, transverse (along-track), and normal (cross-track) directions, respectively. Public LEO orbit errors are strongly direction-dependent, with transverse uncertainty typically dominating the radial and normal components (El-Mowafy et al., 2023; Khairallah & Kassas, 2024; Levit & Marshall, 2011; Wang et al., 2022). This anisotropy is natural in the RTN frame and becomes time-varying and less interpretable in the ECEF frame. Accordingly, the RTN position and velocity errors $\delta \boldsymbol{p}^s_{\mathrm{RTN}}, \delta \boldsymbol{v}^s_{\mathrm{RTN}} \in \mathbb{R}^3$ are modeled as zero-mean Gaussian random vectors:

$$\delta \boldsymbol{p}^s_{\mathrm{RTN}} \sim \mathcal{N}\left(\boldsymbol{0}, \Sigma^s_{\mathrm{RTN},p}\right), \qquad \delta \boldsymbol{v}^s_{\mathrm{RTN}} \sim \mathcal{N}\left(\boldsymbol{0}, \Sigma^s_{\mathrm{RTN},v}\right) \tag{27}$$

where $\Sigma^s_{\mathrm{RTN},p} \in \mathbb{R}^{3\times3}$ and $\Sigma^s_{\mathrm{RTN},v} \in \mathbb{R}^{3\times3}$ describe the covariance matrices of the true orbit error in the RTN frame. For public orbit products, the transverse variance is typically larger than the radial and normal variances; thus, this direction dependence is represented directly in the RTN frame (El-Mowafy et al., 2023; Wang et al., 2022). The general formulation allows a non-diagonal RTN covariance. The position covariance includes correlation between the radial and transverse components:

$$\Sigma^s_{\mathrm{RTN},p} = \mathbf{D}_p^{1/2}\mathbf{C}_p\left(\rho_{\mathrm{RT}}\right)\mathbf{D}_p^{1/2}, \qquad \mathbf{D}_p = \mathrm{diag}\left(\sigma_{\mathrm{R}}^2, \sigma_{\mathrm{T}}^2, \sigma_{\mathrm{N}}^2\right)$$
$$\mathbf{C}_p\left(\rho_{\mathrm{RT}}\right) = \begin{bmatrix} 1 & \rho_{\mathrm{RT}} & 0 \\ \rho_{\mathrm{RT}} & 1 & 0 \\ 0 & 0 & 1 \end{bmatrix} \tag{28}$$

where $\rho_{\mathrm{RT}} \in [-1,1]$ in $\mathbf{C}_p$ is the correlation between the two dominant in-plane components. The diagonal position covariance used in the main experiments is recovered by setting $\rho_{\mathrm{RT}} = 0$. Errors in the normal direction are primarily associated with out-of-plane perturbations, whereas errors in the radial and transverse directions evolve mainly in the orbital plane (Khairallah & Kassas, 2024). Accordingly, only the correlation between the radial and transverse components is retained in this parameterization. The RTN velocity covariance is defined analogously from its three component variances. With $\Sigma^s_{\mathrm{RTN},pv} \triangleq \mathrm{Cov}\left(\delta\boldsymbol{p}^s_{\mathrm{RTN}}, \delta\boldsymbol{v}^s_{\mathrm{RTN}}\right)$, the position and velocity errors likewise admit a per-axis covariance:

$$\Sigma^s_{\mathrm{RTN},pv} = \mathrm{diag}\left(\rho_{pv}\sigma_{\mathrm{R}}\sigma_{v\mathrm{R}}, \rho_{pv}\sigma_{\mathrm{T}}\sigma_{v\mathrm{T}}, \rho_{pv}\sigma_{\mathrm{N}}\sigma_{v\mathrm{N}}\right) \tag{29}$$

with $\rho_{pv} \in [-1,1]$. To map these RTN statistics into the ECEF frame, let the RTN basis at the transmission time be defined for satellite s using its nominal ECEF position $\boldsymbol{p}^s_{\mathrm{ECEF}}(t)$ and its Earth-centered inertial (ECI) velocity vector $\boldsymbol{v}^s_{\mathrm{ECI}}(t) = \boldsymbol{v}^s_{\mathrm{ECEF}}(t) + \boldsymbol{\omega}_e \times \boldsymbol{p}^s_{\mathrm{ECEF}}(t)$, where $\boldsymbol{\omega}_e$ is the Earth's angular velocity vector:

$$\boldsymbol{e}^s_{\mathrm{R}}(t) = \frac{\boldsymbol{p}^s_{\mathrm{ECEF}}(t)}{\|\boldsymbol{p}^s_{\mathrm{ECEF}}(t)\|} \tag{30}$$

$$\boldsymbol{e}^s_{\mathrm{N}}(t) = \frac{\boldsymbol{p}^s_{\mathrm{ECEF}}(t) \times \boldsymbol{v}^s_{\mathrm{ECI}}(t)}{\|\boldsymbol{p}^s_{\mathrm{ECEF}}(t) \times \boldsymbol{v}^s_{\mathrm{ECI}}(t)\|} \tag{31}$$

$$\boldsymbol{e}^s_{\mathrm{T}}(t) = \boldsymbol{e}^s_{\mathrm{N}}(t) \times \boldsymbol{e}^s_{\mathrm{R}}(t) \tag{32}$$

We construct the time-varying rotation matrix:

$$\mathbf{R}^s(t) = \left[\boldsymbol{e}^s_{\mathrm{R}}(t) \quad \boldsymbol{e}^s_{\mathrm{T}}(t) \quad \boldsymbol{e}^s_{\mathrm{N}}(t)\right] \tag{33}$$

The radial, transverse, and normal unit vectors $\boldsymbol{e}^s_{\mathrm{R}}(t), \boldsymbol{e}^s_{\mathrm{T}}(t)$, and $\boldsymbol{e}^s_{\mathrm{N}}(t)$, respectively, form the columns of $\mathbf{R}^s(t) \in \mathbb{R}^{3\times3}$, which maps RTN coordinates into the ECEF frame at epoch t. Here, the ECI velocity is used to define the orbit normal, preventing the transverse and normal directions from being skewed by Earth's rotation. At each epoch, an orbit error expressed in the RTN frame is mapped into the ECEF frame as follows:

$$\delta\boldsymbol{p}^s_{\mathrm{ECEF}}(t) = \mathbf{R}^s(t)\delta\boldsymbol{p}^s_{\mathrm{RTN}} \tag{34}$$

In Equation (34), $\delta\boldsymbol{p}^s_{\mathrm{RTN}} = \left[\delta p^s_{\mathrm{R}}, \delta p^s_{\mathrm{T}}, \delta p^s_{\mathrm{N}}\right]^{\mathrm{T}} \in \mathbb{R}^3$ denotes the orbit error vector resolved in the RTN frame, whereas $\delta\boldsymbol{p}^s_{\mathrm{ECEF}}(t) \in \mathbb{R}^3$ is the same error expressed in

the ECEF frame at epoch t. Because LEO satellites move rapidly across the sky, this rotation varies much faster than in MEO systems. As a result, even when the orbit error remains correlated in the RTN frame, its effect in the observation domain can still change rapidly from epoch to epoch.

Furthermore, the time variation of the RTN basis is described by the skew symmetric matrix:

$$\begin{aligned}\boldsymbol{\Omega}^s(t) &\triangleq \dot{\mathbf{R}}^s(t)\mathbf{R}^s(t)^{\mathrm{T}} = \left[\boldsymbol{\omega}_{\mathrm{RTN}}^{\mathrm{ECEF},s}(t)\right]_\times \\ &= \begin{bmatrix} 0 & -\omega_{\mathrm{Z}}^s(t) & \omega_{\mathrm{Y}}^s(t) \\ \omega_{\mathrm{Z}}^s(t) & 0 & -\omega_{\mathrm{X}}^s(t) \\ -\omega_{\mathrm{Y}}^s(t) & \omega_{\mathrm{X}}^s(t) & 0 \end{bmatrix}\end{aligned} \tag{35}$$

where $\boldsymbol{\omega}_{\mathrm{RTN}}^{\mathrm{ECEF},s}(t) = \left[\omega_{\mathrm{X}}^s(t), \omega_{\mathrm{Y}}^s(t), \omega_{\mathrm{Z}}^s(t)\right]^{\mathrm{T}} \in \mathbb{R}^3$ is the instantaneous angular velocity vector of the RTN frame relative to the ECEF frame, expressed in ECEF coordinates. The matrix $\boldsymbol{\Omega}^s(t) \in \mathbb{R}^{3\times 3}$ is denoted by $[\boldsymbol{\omega}_{\mathrm{RTN}}^{\mathrm{ECEF},s}(t)]_\times$. Its action on any $\boldsymbol{x} \in \mathbb{R}^3$ is defined as $[\boldsymbol{\omega}_{\mathrm{RTN}}^{\mathrm{ECEF},s}(t)]_\times \boldsymbol{x} = \boldsymbol{\omega}_{\mathrm{RTN}}^{\mathrm{ECEF},s}(t) \times \boldsymbol{x}$. This quantity is fully determined by the nominal orbit through $\mathbf{R}^s(t)$. For nearly circular LEO orbits, this term may be evaluated directly from the nominal position and ECEF velocity as follows:

$$\boldsymbol{\omega}_{\mathrm{RTN}}^{\mathrm{ECEF},s}(t) \approx \frac{\boldsymbol{p}_{\mathrm{ECEF}}^s(t) \times \boldsymbol{v}_{\mathrm{ECEF}}^s(t)}{\| \boldsymbol{p}_{\mathrm{ECEF}}^s(t) \|^2} \tag{36}$$

This expression is exact for circular motion and provides the frame rate term used in the covariance propagation in Equations (37) and (39). Because $\mathbf{R}^s(t)$ is an orthogonal rotation matrix, $\mathbf{R}^s(t)^{\mathrm{T}}\mathbf{R}^s(t) = \mathbf{I}$. Multiplying the definition of $\boldsymbol{\Omega}^s(t)$ by $\mathbf{R}^s(t)$ therefore gives $\dot{\mathbf{R}}^s(t) = \boldsymbol{\Omega}^s(t)\mathbf{R}^s(t)$. The corresponding ECEF velocity perturbation $\delta\boldsymbol{v}_{\mathrm{ECEF}}^s(t) \in \mathbb{R}^3$ is as follows:

$$\begin{aligned}\delta\boldsymbol{v}_{\mathrm{ECEF}}^s(t) &= \mathbf{R}^s(t)\delta\boldsymbol{v}_{\mathrm{RTN}}^s + \dot{\mathbf{R}}^s(t)\delta\boldsymbol{p}_{\mathrm{RTN}}^s \\ &= \mathbf{R}^s(t)\delta\boldsymbol{v}_{\mathrm{RTN}}^s + \boldsymbol{\Omega}^s(t)\mathbf{R}^s(t)\delta\boldsymbol{p}_{\mathrm{RTN}}^s \\ &= \mathbf{R}^s(t)\delta\boldsymbol{v}_{\mathrm{RTN}}^s + \boldsymbol{\Omega}^s(t)\delta\boldsymbol{p}_{\mathrm{ECEF}}^s(t)\end{aligned} \tag{37}$$

Equation (37) gives the kinematic relation for the ECEF velocity perturbation. Its second term accounts for RTN frame rotation and is especially important for LEO satellites, because even a static RTN position bias induces a noticeable apparent velocity change when represented in the ECEF frame (Khairallah & Kassas, 2024).

With the general RTN correlations of Equations (28)–(29), the ECEF position covariance is as follows:

$$\boldsymbol{\Sigma}_p^s(t) = \mathbf{R}^s(t)\boldsymbol{\Sigma}_{\mathrm{RTN},p}^s\mathbf{R}^s(t)^{\mathrm{T}} \tag{38}$$

The corresponding ECEF velocity covariance is as follows:

$$\begin{aligned}\boldsymbol{\Sigma}_v^s(t) = {} & \mathbf{R}^s(t)\boldsymbol{\Sigma}_{\mathrm{RTN},v}^s\mathbf{R}^s(t)^{\mathrm{T}} \\ & + \boldsymbol{\Omega}^s(t)\mathbf{R}^s(t)\boldsymbol{\Sigma}_{\mathrm{RTN},p}^s\mathbf{R}^s(t)^{\mathrm{T}}\boldsymbol{\Omega}^s(t)^{\mathrm{T}} \\ & + \mathbf{R}^s(t)\boldsymbol{\Sigma}_{\mathrm{RTN},pv}^{s\mathrm{T}}\mathbf{R}^s(t)^{\mathrm{T}}\boldsymbol{\Omega}^s(t)^{\mathrm{T}} \\ & + \boldsymbol{\Omega}^s(t)\mathbf{R}^s(t)\boldsymbol{\Sigma}_{\mathrm{RTN},pv}^s\mathbf{R}^s(t)^{\mathrm{T}}\end{aligned} \tag{39}$$

The same rotation induces the ECEF position velocity covariance:

$$\begin{aligned}\Sigma^{s}_{pv}(t) &\triangleq \mathrm{Cov}\left(\delta \boldsymbol{p}^{s}_{\mathrm{ECEF}}(t), \delta \boldsymbol{v}^{s}_{\mathrm{ECEF}}(t)\right) \\ &= \mathbf{R}^{s}(t)\Sigma^{s}_{\mathrm{RTN},pv}\mathbf{R}^{s}(t)^{\mathrm{T}} + \Sigma^{s}_{p}(t)\boldsymbol{\Omega}^{s}(t)^{\mathrm{T}}\end{aligned} \tag{40}$$

Even when $\Sigma^{s}_{\mathrm{RTN},pv} = \mathbf{0}$, the frame rotation term $\Sigma^{s}_{p}(t)\boldsymbol{\Omega}^{s}(t)^{\mathrm{T}}$ remains nonzero.

3.2 | Joint Observation-Domain Covariance Construction

We now propagate the per-satellite ECEF perturbations in Equations (34) and (37), together with their covariance matrices in Equations (38)–(40), into the SD and DD observation domains. The nominal carrier-phase and Doppler stochastic model has already been defined in Section 2; here, we derive only the additional covariance caused by ephemeris uncertainty. The final observation covariance is obtained by adding this orbit-induced increment to the nominal covariance.

3.2.1 | SD Covariance Construction

Let the tracked satellites at a common epoch be ordered as $\{s_0, s_1, \ldots, s_m\}$, where s_0 is the reference satellite. For each satellite, Equations (38)–(40) provide the ECEF position covariance, velocity covariance, and position–velocity cross-covariance blocks $\Sigma^{s}_{p}, \Sigma^{s}_{v}$, and $\Sigma^{s}_{pv} \in \mathbb{R}^{3\times 3}$. Stacking all satellites yields the following:

$$\Sigma_{p} = \mathrm{blkdiag}\left(\Sigma^{s_0}_{p}, \Sigma^{s_1}_{p}, \ldots, \Sigma^{s_m}_{p}\right) \tag{41}$$

$$\Sigma_{v} = \mathrm{blkdiag}\left(\Sigma^{s_0}_{v}, \Sigma^{s_1}_{v}, \ldots, \Sigma^{s_m}_{v}\right) \tag{42}$$

$$\Sigma_{pv} = \mathrm{blkdiag}\left(\Sigma^{s_0}_{pv}, \Sigma^{s_1}_{pv}, \ldots, \Sigma^{s_m}_{pv}\right) \tag{43}$$

The block diagonal form in Equation (43) assumes mutually independent orbit errors across satellites. This form is used when inter-satellite covariance information is unavailable. Public TLE products are a typical example. For coplanar LEO satellites propagated from TLE/SGP4, orbit errors may contain plane-level common components and satellite-specific components. Common components enter the stacked SD covariance before differencing. When the SD observables are later transformed to DD, components shared by the current and reference satellites partly cancel, while satellite-specific components remain. Correspondingly, we define the stacked ECEF orbit error perturbation vectors:

$$\delta \boldsymbol{p}_{\mathrm{orb}} = \left[\left(\delta \boldsymbol{p}^{s_0}_{\mathrm{ECEF}}\right)^{\mathrm{T}} \quad \left(\delta \boldsymbol{p}^{s_1}_{\mathrm{ECEF}}\right)^{\mathrm{T}} \quad \cdots \quad \left(\delta \boldsymbol{p}^{s_m}_{\mathrm{ECEF}}\right)^{\mathrm{T}}\right]^{\mathrm{T}} \tag{44}$$

$$\delta \boldsymbol{v}_{\mathrm{orb}} = \left[(\delta \boldsymbol{v}^{s_0}_{\mathrm{ECEF}})^{\mathrm{T}} \quad (\delta \boldsymbol{v}^{s_1}_{\mathrm{ECEF}})^{\mathrm{T}} \quad \cdots \quad (\delta \boldsymbol{v}^{s_m}_{\mathrm{ECEF}})^{\mathrm{T}}\right]^{\mathrm{T}} \tag{45}$$

where each satellite block is obtained from the RTN-to-ECEF mappings in Equations (34) and (37). Thus, $\delta \boldsymbol{p}_{\mathrm{orb}}$ and $\delta \boldsymbol{v}_{\mathrm{orb}}$ are stacked versions of the single-satellite perturbations introduced in Section 3.1. The subscript "orb" avoids confusion with the receiver state corrections $\delta \boldsymbol{p}$ and $\delta \boldsymbol{v}$ in Section 2.3. Under

the independence assumption adopted above, their covariance matrices are $\mathrm{Cov}(\delta \boldsymbol{p}_{\mathrm{orb}}) = \Sigma_p$ and $\mathrm{Cov}(\delta \boldsymbol{v}_{\mathrm{orb}}) = \Sigma_v$, with $\mathrm{Cov}(\delta \boldsymbol{p}_{\mathrm{orb}}, \delta \boldsymbol{v}_{\mathrm{orb}}) = \Sigma_{pv}$. We now project these stacked orbit errors into the SD and DD observation domains. At the SD level, the orbit-induced carrier-phase perturbation for satellite s is driven by the rover–base viewing direction difference (Khalife & Kassas, 2023; Zhao et al., 2023):

$$\boldsymbol{a}^s = \boldsymbol{u}_b^s - \boldsymbol{u}_r^s \in \mathbb{R}^3 \tag{46}$$

which is the SD phase sensitivity to orbit error. The Doppler perturbation contains both a velocity projection term with the same SD sensitivity and a position-driven rate term. Following the implemented residual sign convention, the latter is written as follows (Baron et al., 2024; Zhao et al., 2023):

$$\boldsymbol{c}^s = -\left[\left(\frac{\boldsymbol{v}_{\mathrm{ECEF}}^s - \boldsymbol{v}_r}{\rho_r^s} - \frac{\left(\boldsymbol{v}_{\mathrm{ECEF}}^s - \boldsymbol{v}_r\right)^{\mathrm{T}} \boldsymbol{\rho}_r^s}{\left(\rho_r^s\right)^3} \boldsymbol{\rho}_r^s\right) - \left(\frac{\boldsymbol{v}_{\mathrm{ECEF}}^s - \boldsymbol{v}_b}{\rho_b^s} - \frac{\left(\boldsymbol{v}_{\mathrm{ECEF}}^s - \boldsymbol{v}_b\right)^{\mathrm{T}} \boldsymbol{\rho}_b^s}{\left(\rho_b^s\right)^3} \boldsymbol{\rho}_b^s\right)\right] \tag{47}$$

Here, $\boldsymbol{c}^s \in \mathbb{R}^3$. The vectors $\boldsymbol{\rho}_r^s$ and $\boldsymbol{\rho}_b^s \in \mathbb{R}^3$ denote the rover-to-satellite and base-to-satellite geometric vectors, with $\rho_r^s = \| \boldsymbol{\rho}_r^s \|$ and $\rho_b^s = \| \boldsymbol{\rho}_b^s \|$, and $\boldsymbol{v}_r$ and $\boldsymbol{v}_b \in \mathbb{R}^3$ are the rover and base velocities, respectively. When the user receiver is static, its contribution disappears because $\boldsymbol{v}_r = \boldsymbol{0}$; if the base is also static, the corresponding base term disappears as well, and the expression reduces to the static case. These sensitivities also explain why SD suppresses orbit error. Because $\boldsymbol{a}^s$ is the difference between the rover and base line-of-sight vectors to the same satellite, only the noncommon part of the orbit error appears in Equation (51). In the zero-baseline limit, $\boldsymbol{u}_b^s = \boldsymbol{u}_r^s$ and thus $\boldsymbol{a}^s = \boldsymbol{0}$; if the rover and base also have the same instantaneous kinematics, then $\boldsymbol{c}^s = \boldsymbol{0}$ as well. Hence, the common satellite orbit error is fully canceled in the zero-baseline case and grows only as the rover and base geometry separates. In the LEO case, this baseline effect is further influenced by the rapidly changing observation geometry caused by the fast satellite motion. We define the SD sensitivity matrices as block diagonal row operators:

$$\mathbf{A}_{\varphi,\mathrm{SD}} = \mathrm{blkdiag}\left(\left(\boldsymbol{a}^{s_0}\right)^{\mathrm{T}}, \left(\boldsymbol{a}^{s_1}\right)^{\mathrm{T}}, \ldots, \left(\boldsymbol{a}^{s_m}\right)^{\mathrm{T}}\right) \tag{48}$$

$$\mathbf{A}_{d,v,\mathrm{SD}} = \mathbf{A}_{\varphi,\mathrm{SD}} \tag{49}$$

$$\mathbf{A}_{d,p,\mathrm{SD}} = \mathrm{blkdiag}\left(\left(\boldsymbol{c}^{s_0}\right)^{\mathrm{T}}, \left(\boldsymbol{c}^{s_1}\right)^{\mathrm{T}}, \ldots, \left(\boldsymbol{c}^{s_m}\right)^{\mathrm{T}}\right) \tag{50}$$

so that the corresponding SD orbit-induced measurement perturbations follow from a Taylor-series expansion of the observation equations about the nominal satellite state, in which only the first-order term is retained. These perturbations can therefore be written as follows:

$$\delta \boldsymbol{y}_{\varphi,\mathrm{orb,SD}} = \mathbf{A}_{\varphi,\mathrm{SD}}\, \delta \boldsymbol{p}_{\mathrm{orb}} \tag{51}$$

$$\delta \boldsymbol{y}_{d,\mathrm{orb,SD}} = \mathbf{A}_{d,v,\mathrm{SD}}\, \delta \boldsymbol{v}_{\mathrm{orb}} + \mathbf{A}_{d,p,\mathrm{SD}}\, \delta \boldsymbol{p}_{\mathrm{orb}} \tag{52}$$

Equations (34) and (37) map the RTN orbit error into per-satellite ECEF position and velocity errors. Equations (51) and (52) then project their stacked forms into

SD phase and Doppler perturbations. With $\mathrm{Cov}\left(\delta \boldsymbol{p}_{\mathrm{orb}}\right)=\Sigma_{p}$, $\mathrm{Cov}\left(\delta \boldsymbol{v}_{\mathrm{orb}}\right)=\Sigma_{v}$, and $\mathrm{Cov}\left(\delta \boldsymbol{p}_{\mathrm{orb}}, \delta \boldsymbol{v}_{\mathrm{orb}}\right)=\Sigma_{pv}$, the SD orbit-induced covariance blocks are as follows:

$$\Sigma_{\varphi\varphi,\mathrm{orb,SD}} = \mathbf{A}_{\varphi,\mathrm{SD}} \Sigma_{p} \mathbf{A}_{\varphi,\mathrm{SD}}^{\mathrm{T}} \tag{53}$$

$$\begin{aligned} \Sigma_{dd,\mathrm{orb,SD}} = {} & \mathbf{A}_{d,v,\mathrm{SD}} \Sigma_{v} \mathbf{A}_{d,v,\mathrm{SD}}^{\mathrm{T}} + \mathbf{A}_{d,p,\mathrm{SD}} \Sigma_{p} \mathbf{A}_{d,p,\mathrm{SD}}^{\mathrm{T}} \\ & + \mathbf{A}_{d,p,\mathrm{SD}} \Sigma_{pv} \mathbf{A}_{d,v,\mathrm{SD}}^{\mathrm{T}} + \mathbf{A}_{d,v,\mathrm{SD}} \Sigma_{pv}^{\mathrm{T}} \mathbf{A}_{d,p,\mathrm{SD}}^{\mathrm{T}} \end{aligned} \tag{54}$$

$$\Sigma_{\varphi d,\mathrm{orb,SD}} = \mathbf{A}_{\varphi,\mathrm{SD}} \Sigma_{p} \mathbf{A}_{d,p,\mathrm{SD}}^{\mathrm{T}} + \mathbf{A}_{\varphi,\mathrm{SD}} \Sigma_{pv} \mathbf{A}_{d,v,\mathrm{SD}}^{\mathrm{T}} \tag{55}$$

The cross-covariance terms above are present even when an orbit product supplies only separate RTN position and velocity uncertainty blocks, because the frame-induced component in Equation (40) is determined by the nominal orbit. If a product also supplies an intrinsic $\Sigma_{\mathrm{RTN},pv}$, its rotated contribution is added through the first term of Equation (40). Equations (53)–(55) describe only the orbit-induced SD covariance increment. These equations also make the source of the covariance clear: phase is driven by position uncertainty, whereas Doppler is driven by both velocity uncertainty and the time variation of the viewing geometry. The cross block $\Sigma_{\varphi d,\mathrm{orb,SD}}$ captures the same-epoch correlation between phase residuals and Doppler perturbations caused by the same orbit error, thereby keeping the joint update sign consistent. When the position component of orbit error varies slowly relative to the observation interval, this distinction also explains why Doppler is usually less sensitive than phase. Equations (51) and (53) show that the phase component depends directly on the orbit position bias and its covariance, whereas Equations (52) and (54) show that the Doppler component depends on the induced velocity error and the time variation of the line-of-sight projection. As a result, a slowly varying position bias typically produces a stronger disturbance in the range domain than in the rate domain. The corresponding orbit-induced SD joint covariance is as follows:

$$\Sigma_{\mathrm{orb,SD}} = \begin{bmatrix} \Sigma_{\varphi\varphi,\mathrm{orb,SD}} & \Sigma_{\varphi d,\mathrm{orb,SD}} \\ \Sigma_{\varphi d,\mathrm{orb,SD}}^{\mathrm{T}} & \Sigma_{dd,\mathrm{orb,SD}} \end{bmatrix} \tag{56}$$

The final SD observation covariance can then be written as follows:

$$\Sigma_{\mathrm{SD}} = \Sigma_{\mathrm{nom,SD}} + \Sigma_{\mathrm{orb,SD}} \tag{57}$$

3.2.2 | DD Transformation and Joint Covariance

Once the SD orbit perturbations and covariance increment are assembled, the DD orbit perturbations follow from the same linear transformation introduced in Equation (23):

$$\delta \boldsymbol{y}_{\varphi,\mathrm{orb,DD}} = \mathbf{D}\, \delta \boldsymbol{y}_{\varphi,\mathrm{orb,SD}} \tag{58}$$

$$\delta \boldsymbol{y}_{d,\mathrm{orb,DD}} = \mathbf{D}\, \delta \boldsymbol{y}_{d,\mathrm{orb,SD}} \tag{59}$$

That is, the DD orbit perturbations are the SD perturbations after application of the differencing operator to each observable type. Taking the covariance of Equation (59) gives the DD covariance blocks:

$$\Sigma_{\varphi\varphi,\mathrm{orb,DD}} = \mathbf{D}\,\Sigma_{\varphi\varphi,\mathrm{orb,SD}}\,\mathbf{D}^{\mathrm{T}} \tag{60}$$

$$\Sigma_{dd,\mathrm{orb,DD}} = \mathbf{D}\,\Sigma_{dd,\mathrm{orb,SD}}\,\mathbf{D}^{\mathrm{T}} \tag{61}$$

$$\Sigma_{\varphi d,\mathrm{orb,DD}} = \mathbf{D}\,\Sigma_{\varphi d,\mathrm{orb,SD}}\,\mathbf{D}^{\mathrm{T}} \tag{62}$$

Equation (62) introduces the two ingredients required by the DD model in Section 2.3: the shared contribution of the reference satellite and the covariance mapping from SD observables to DD observables. The position–velocity cross-covariance is already contained in the SD blocks and therefore undergoes the same joint blkdiag($\mathbf{D}$, $\mathbf{D}$) transformation. In this way, the DD covariance is not an additional assumption, but a direct image of the SD covariance under $\mathbf{D}$. Note that $\boldsymbol{a}^s = \boldsymbol{u}_b^s - \boldsymbol{u}_r^s$ in Section 3.1 represents the between-receiver projection for satellite s. The DD operator $\mathbf{D}$ subtracts the corresponding projection of reference satellite s_0, thereby completing the two-satellite construction and introducing the reference satellite covariance into every DD row. These equations also explain why DD can enlarge the orbit-induced error relative to SD. Each DD observable is formed by subtracting a reference satellite SD term from the current satellite SD term; thus, the reference satellite covariance contribution appears in every DD row through Equation (59). For the simplified case in which SD orbit terms of different satellites are treated as independent, this approach gives $\mathrm{Var}\left(\delta y^s_{\mathrm{orb,DD}}\right) = \mathrm{Var}\left(\delta y^s_{\mathrm{orb,SD}}\right) + \mathrm{Var}\left(\delta y^{s_0}_{\mathrm{orb,SD}}\right)$, directly showing that a poor reference satellite can inflate the covariance of the entire DD set. Thus, reference satellite selection should consider the projected orbit covariance in addition to elevation and signal quality.

The carrier-phase and Doppler orbit increments are then combined through the joint covariance matrix:

$$\Sigma_{\mathrm{orb,DD}} = \begin{bmatrix} \Sigma_{\varphi\varphi,\mathrm{orb,DD}} & \Sigma_{\varphi d,\mathrm{orb,DD}} \\ \Sigma^{\mathrm{T}}_{\varphi d,\mathrm{orb,DD}} & \Sigma_{dd,\mathrm{orb,DD}} \end{bmatrix} \tag{63}$$

When the same-epoch full-covariance option is enabled, Equations (53)–(63) are evaluated for all satellites in the epoch; thus, the resulting matrix preserves both the DD reference satellite coupling and the same satellite phase and Doppler cross-correlation across all rows. This preservation serves as the mathematical basis of the joint update in the current implementation. The final DD observation covariance is obtained by adding this orbit-induced increment to the nominal DD covariance derived in Section 2.3:

$$\Sigma_{\mathrm{DD}} = \Sigma_{\mathrm{nom,DD}} + \Sigma_{\mathrm{orb,DD}} \tag{64}$$

Thus, the final DD covariance in Equation (64) combines the nominal measurement covariance from Section 2.1 with the orbit-induced covariance derived above. The former represents the assumed random measurement noise model, whereas the latter accounts for the same-epoch covariance generated by common satellite orbit errors.

4 | EXPERIMENTS AND RESULTS

This section evaluates the proposed framework through simulation experiments. We first introduce the common simulation setup and then compare the performance with and without OUCA, across observation modes under OUCA, and across SD and DD architectures.

4.1 | Experimental Setup and Simulation Design

Table 1 summarizes the common simulation settings.

Using these error models, we conducted 2700 paired navigation scenarios. The rover and base are static. The rover truth position is approximately 32.67°N, 116.22°E, with an ellipsoidal height of 4.58 km, and the base position is generated using the prescribed baseline. The design combines three orbit precision grades, three baselines of 5, 10, and 50 km, and three observation modes. For each configuration, 100 independent Monte Carlo tests were applied to characterize the mean performance and its variability. Satellite truth states were propagated with SGP4 from a Starlink-style TLE catalog. The SD and DD matrices retain only visible satellites. At each epoch, satellites below the 20° elevation mask are excluded. The number of retained satellites varies from 71 to 80 over each 2-min arc, with an epoch-averaged value of 75.2.

For the simulation, the satellite position and velocity propagated by SGP4 in the true-equator mean-equinox frame are transformed to the ECEF frame and used as truth states in the controlled simulation. These states are used to generate the phase and Doppler observations from the nonlinear signal flight time geometry. The observations include atmospheric delays, receiver and satellite clock errors, integer ambiguities, Sagnac and relativistic corrections, and measurement noise. The simulated RTN position and velocity errors are mapped to the ECEF frame and added to the truth states to construct the erroneous ephemeris supplied to the estimator. Therefore, the orbit-induced residual arises from the difference between observations generated with the true satellite states and predictions formed from the erroneous ephemeris. The first-order projection derived in Section 3 is used only to propagate the orbit covariance into the observation domain for OUCA.

TABLE 1
Configuration Parameters for the Monte Carlo Simulation Framework

Parameter	Value/Description
Satellite Constellation	Starlink-style TLE catalog, truth states propagated via SGP4
Test Site	Fixed simulated site at approximately 32.67°N, 116.22°E, $h \approx 4.58$ km
User Motion	Static rover and static base
Simulation Duration	120 s per test
Measurement Rate	1 Hz
Carrier Frequency	Single 10.7-GHz carrier ($\lambda \approx 2.8$ cm)
Measurement Noise (Thermal)	Link-dependent; reference standard deviations at 550 km: 3 mm (phase), 0.05 m/s (Doppler)
Estimator Architecture	EKF with OUCA

4.1.1 | Orbital Error Generation

We represent satellite ephemeris quality with three grades: decimeter, meter, and TLE. The TLE grade denotes standard general perturbation elements, which are the least accurate public orbit source considered here. More accurate public products include supplemental general perturbation elements and operator-provided Starlink ephemerides published by SpaceX (A.-r. Liu et al., 2025). These products may provide orbit accuracy between the meter and TLE grades (Khairallah & Kassas, 2024). The orbit errors are generated in the RTN frame and mapped to the ECEF frame. The grades differ only in covariance magnitude. For the decimeter and meter grades, the position standard deviations are isotropic and set to 0.1 m and 1.5 m, respectively (El-Mowafy et al., 2023; S. Yang et al., 2025). For the TLE grade, the RTN standard deviations are approximately [300, 2640, 600] m for position and [0.3, 1.2, 0.2] m/s for velocity. These values preserve the dominant transverse uncertainty reported in the LEO orbit prediction literature (El-Mowafy et al., 2023; Khairallah & Kassas, 2024; Levit & Marshall, 2011). Note that the adopted TLE grade represents a fixed short-term uncertainty level rather than a covariance for one specific ephemeris age. An assessment of approximately 6300 Starlink satellites reported a median three-dimensional (3D) TLE position error of 1.01 km at epoch. For satellites in the station-keeping phase, the median transverse error increased to 1.95 km after 8 h and 6.77 km after 24 h (Huang et al., 2026). These results place the adopted transverse uncertainty within the observed kilometer-level range for recent TLEs. The results also show that practical orbit uncertainty depends on ephemeris age and orbital phase. The quoted [0.3, 1.2, 0.2] m/s values are the intrinsic RTN drift-rate components $\delta\boldsymbol{v}^s_{\mathrm{RTN}}$ of Equation (65). The total ephemeris velocity error also contains the frame-rotation coupling $\boldsymbol{\Omega}^s(t)\delta\boldsymbol{p}^s_{\mathrm{ECEF}}(t)$ of Equation (37). This term maps the transverse position error into a radial velocity error of magnitude $n\,\sigma_{\mathrm{T}} \approx 2.9$ m/s, where n is the mean motion. The resulting simulated velocity error is radial-dominant, consistent with reported LEO ephemeris error statistics. Ephemeris errors arise from differences between propagated orbital states and evolve smoothly over short prediction intervals (Khairallah & Kassas, 2024; Levit & Marshall, 2011). Over 2 min, a typical LEO satellite at approximately 550-km altitude traverses only about 7°–8° of its orbit, or roughly 2% of a 95-min orbital period. Thus, the per-satellite RTN error is represented by the following first-order local model over each simulation arc:

$$\delta\boldsymbol{p}^s_{\mathrm{RTN}}(t) = \delta\boldsymbol{p}^s_{\mathrm{RTN},0} + \delta\boldsymbol{v}^s_{\mathrm{RTN}}t \tag{65}$$

where the initial offset $\delta\boldsymbol{p}^s_{\mathrm{RTN},0} \sim \mathcal{N}\left(\mathbf{0}, \Sigma^s_{\mathrm{RTN},p}\right)$ is generated once for each satellite in each arc (Khairallah & Kassas, 2024) and $\delta\boldsymbol{v}^s_{\mathrm{RTN}}$ is a per-satellite RTN drift rate. The velocity error is the exact derivative $\delta\dot{\boldsymbol{p}}^s_{\mathrm{RTN}} = \delta\boldsymbol{v}^s_{\mathrm{RTN}}$; thus, the injected position and velocity errors remain kinematically consistent through Equation (37). The error is Gaussian only in the ensemble sense across Monte Carlo realizations of $\delta\boldsymbol{p}^s_{\mathrm{RTN},0}$. Within each arc, a given realization is a deterministic constant plus a drift error whose time average over the arc is generally nonzero. Therefore, the estimator faces a systematic bias rather than noise that averages toward zero. The main experiments use diagonal $\Sigma_{\mathrm{RTN},p}$, with $\Sigma_{\mathrm{RTN},pv} = \mathbf{0}$. In Section 4.5, nonzero RTN and position velocity correlations are injected while this filter model is retained to quantify sensitivity to the mismatch. The simulated orbit error remains strongly time-correlated in the RTN frame, whereas its effect in the observation domain still changes from epoch to epoch through the rapidly varying LEO geometry.

4.1.2 | Atmospheric Modeling

A representative carrier frequency of 10.7 GHz is used in the simulations, as listed in Table 1. This value lies at the lower edge of the reported Starlink Ku-band downlink range and is therefore adopted here as a representative broadband signal-of-opportunity (SoOP) frequency (Allahvirdi-Zadeh et al., 2025; Humphreys et al., 2023). At such frequencies, the first-order ionospheric effect is much smaller than in GNSS bands, and under the short-baseline differential setup, the remaining atmospheric terms are secondary. At 10.7 GHz, 1 TECU (total electron content unit) gives approximately 3.5 mm of first-order ionospheric delay. For the longest 50-km baseline considered here, a differential slant TEC residual below approximately 0.28 TECU produces a sub-millimeter-range effect. This finding is consistent with the Ku-band analysis reported by Allahvirdi-Zadeh et al. (2025), where free-space attenuation dominated the propagation loss and cloud and fog losses were comparatively small.

Thus, the simulation represents residual atmospheric effects without introducing a full broadband propagation model. Following LEO differential positioning analyses, residual atmospheric effects are treated as baseline-dependent terms that are strongly reduced over short baselines but can grow as the rover–base separation increases (Khalife & Kassas, 2023). Line-of-sight mapping follows the Niell mapping function (Niell, 1996). The residual wet zenith delays at the rover and base are generated as correlated random walks with a process noise standard deviation of 0.001 m per square root epoch. Their correlation decreases exponentially with baseline length based on a 20-km spatial correlation length. The residuals are then mapped to each satellite line of sight. Receiver and satellite differencing produces the baseline-dependent tropospheric residual in the phase observations. The corresponding Doppler residual is obtained by differencing the slant tropospheric delay between consecutive 1-s epochs. The residual ionospheric delays are modeled separately as correlated random walks with a 50-km spatial correlation length and a process noise standard deviation of 0.0002 m per square root epoch. For the carrier phase, the ionosphere enters as a phase advance; thus, the residual slant term is modeled as $-I+T$ in the simulated carrier-phase observable. For the estimation, the atmospheric parameters are not estimated separately for each satellite. For each atmospheric component, one zenith residual is estimated for the rover and one for the base, and these shared parameters are mapped to each satellite line of sight.

4.1.3 | Clock and Noise Profiles

Receiver and satellite clocks are simulated with a simplified stochastic bias drift model rather than a hardware-specific oscillator model. No particular clock type is assumed, because clock effects are almost completely removed by the DD architecture. The clock terms are retained to keep the raw observation simulation realistic before differencing. Each receiver clock is propagated as a two-state random walk at the 1-s epoch rate: the drift accumulates a zero-mean Gaussian increment with a standard deviation of 1 mm/s per epoch, and the bias accumulates the current drift plus a zero-mean Gaussian increment with a standard deviation of 5 cm. The satellite clock uses the same drift increment and a 5-mm bias increment. The rover and base clocks are generated independently, so no part of the receiver clock is common between them.

The observation noise varies with the receiver satellite link. Following the link budget and closed-loop Doppler tracking model reported by

Allahvirdi-Zadeh et al. (2025), the carrier-to-noise-density ratio is computed from free-space loss using an effective isotropic radiated power of 30 dBW and a receiver G/T of 20 dB/K. The Doppler tracking model uses a loop bandwidth of $B_f = 25$ Hz and an integration time of $T = 5$ ms. Carrier-phase and Doppler reference standard deviations of 3 mm and 0.05 m/s are assigned at a 550-km slant range, consistent with reported precision levels for differential LEO observations (Khalife & Kassas, 2023; Psiaki, 2021). For each link, the phase standard deviation is scaled by the square root of the inverse relative C/N_0. The Doppler standard deviation is scaled by the relative closed-loop tracking standard deviation:

$$\sigma^s_{\varphi,r} = 0.003 \max\left(1, \sqrt{\frac{(C/N_0)_{\text{ref}}}{(C/N_0)^s_r}}\right) \text{ m} \tag{66}$$

$$\sigma^s_{d,r} = 0.05 \max\left(1, \frac{\tilde{\sigma}_d((C/N_0)^s_r)}{\tilde{\sigma}_d((C/N_0)_{\text{ref}})}\right) \text{ m/s} \tag{67}$$

where:

$$\tilde{\sigma}_d(C/N_0) = \frac{c}{f}\sqrt{\frac{B_f}{4\pi^2 T^2 (C/N_0)}\left(1 + \frac{1}{T(C/N_0)}\right)} \tag{68}$$

The same link-dependent standard deviations are used to generate the zero-mean Gaussian observation noise and to form the nominal covariance supplied to the estimator. Noise samples are generated independently for each receiver and satellite. For the correlation between the phase and Doppler random noise components, we set $\rho_{\varphi d} = 0$ in the main experiments. This setting follows common GNSS filtering practice in which carrier-phase and Doppler random noise are treated as independent under nominal tracking, while the physical phase–frequency relation is carried by the state dynamics. Because real carrier-phase and Doppler measurements can share tracking and propagation errors, the true $\rho_{\varphi d}$ is varied from −0.8 to 0.8 in Section 4.5, while $\rho_{\varphi d} = 0$ is assumed for the estimator. Section 4.5 shows that this covariance mismatch has no resolvable effect.

4.1.4 | *Deterministic Corrections*

The simulated raw observables include the first-order Sagnac correction for Earth's rotation. These observables also include the standard orbit-dependent satellite clock relativistic correction, written in range units as $-2\left(\boldsymbol{p}^s_{\text{ECEF}}\right)^{\text{T}} \boldsymbol{v}^s_{\text{ECEF}}/c$. No separate gravitational redshift or standalone second-order Doppler state is estimated. The remaining satellite clock effects are removed by differencing. The receive time geometric range and range rate are evaluated consistently with the signal transmission time, so that the remaining residuals studied in this paper are dominated by orbit error, atmosphere, clock instability, and measurement noise rather than by unmodeled deterministic effects.

4.1.5 | *Ambiguity Resolution Setting*

In practical opportunistic SoOP scenarios, public orbit products are imperfect, and the number of actually observed satellites may remain limited even when many

LEO satellites are overhead. For the chosen 10.7-GHz carrier, the wavelength is only approximately 2.8 cm, which is much shorter than typical GNSS wavelengths; thus, ambiguity fixing is intrinsically more difficult in the presence of residual orbit and tracking errors. For this reason, partial ambiguity resolution (PAR) is used to fix only the subset of ambiguities with high expected reliability, while leaving uncertain ambiguities as float instead of forcing a full integer solution.

In the truth model, one integer ambiguity is independently sampled for each satellite and receiver from a uniform distribution over $[-2000, 2000)$ cycles and held constant over the arc. The corresponding DD ambiguity truth is obtained by applying the same DD operation as used for the observations. A fixed ambiguity is considered correct only when it exactly matches this DD truth. The fix rate (FR) and correct fix rate (CFR) are evaluated over the same set of ambiguity candidates.

In the DD estimator, the float ambiguities are ordered by decreasing marginal variance, which places the most precise candidates at the end of the vector. The bootstrap success probability is evaluated while the less precise candidates are removed. The largest trailing subset that reaches the success threshold of $1-10^{-10}$ is fixed by bootstrapping in the original ambiguity space. No ambiguity decorrelation or global integer least-squares search is used. The conditional fixed position is reported for that epoch, while the recursive filter remains as float and repeats PAR at the next epoch.

4.2 | Comparison With and Without OUCA

This subsection compares the main DD estimator without covariance adaptation (nominal) and with covariance adaptation (OUCA) across the three observation modes: phase-only, Doppler-only, and phase+Doppler. Without OUCA, the joint filter places too much trust in orbit-contaminated carrier-phase information in the difficult scenarios; thus, even the phase+Doppler solution can become unstable. With OUCA, orbit uncertainty is mapped into the joint observation covariance. The weighting becomes consistent with the actual uncertainty, and the estimator remains stable across orbit grades and baselines. OUCA improves all three modes. The gain is small in decimeter-grade scenarios, moderate to strong for phase in meter-grade scenarios, and largest in TLE-grade scenarios where orbit uncertainty dominates.

All reported 3D position errors are computed as the Euclidean norm between the estimated rover position and the known position of the static test site, that is, $\|\hat{\boldsymbol{p}}_r - \boldsymbol{p}_r\|_2$. For the final accuracy figures, this metric is evaluated at the last epoch of each 120-s test and then summarized over the 100 tests, whereas the time-series figure shows the same 3D error epoch by epoch.

Figure 1 summarizes the final 3D positioning accuracy over the full three-mode matrix and makes the differences across the three modes explicit. The phase, Doppler, and phase+Doppler results are shown in the top, middle, and bottom panels of the figure, respectively. Under decimeter-grade ephemeris, OUCA leaves the already precise solutions nearly unchanged. Under meter-grade ephemeris, OUCA primarily benefits the phase and phase+Doppler modes. At the 50-km baseline, the phase error decreases from 0.408 to 0.210 m, whereas the phase+Doppler error decreases from 0.213 to 0.097 m. Under TLE-grade ephemeris, all three modes show strong improvement. At the 10-km baseline, the phase+Doppler error decreases from 56.232 to 4.581 m, a reduction of 91.9%. At 50 km, this error decreases from 286.742 to 13.616 m, a reduction of 95.3%. These results show that OUCA benefits each observation mode and supports robust phase+Doppler processing. Table 2 provides the exact TLE-grade values across all modes and baselines.

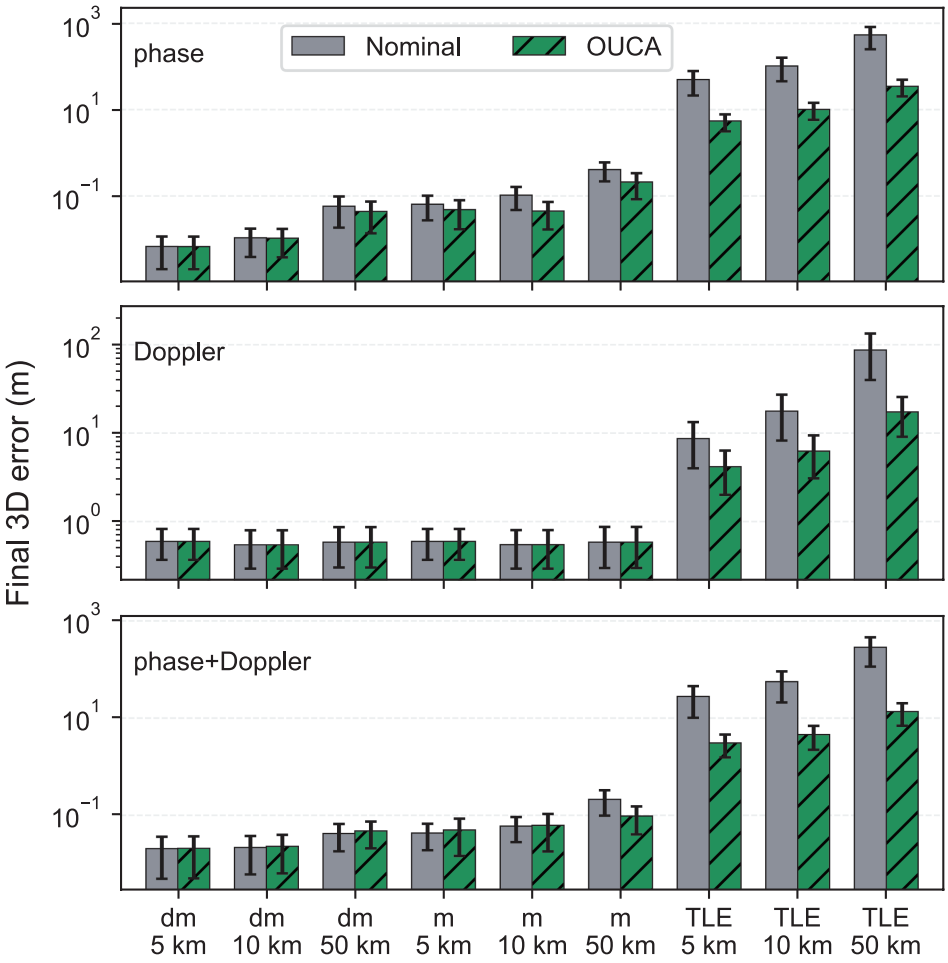

FIGURE 1 Final 3D accuracy of nominal and OUCA results for the phase (top), Doppler (middle), and phase+Doppler (bottom) modes
Compared with the best single-observation mode, the phase+Doppler mode retains the same accuracy level under high-precision orbit conditions and improves positioning accuracy under TLE-grade orbit conditions.

TABLE 2
TLE-Grade Final 3D Positioning Errors for Nominal and OUCA Results Across All DD Observation Modes and Baselines (Mean ± Standard Deviation, Meters)

Mode	Baseline	Nominal (m)	OUCA (m)
phase	5 km	49.620 ± 28.420	5.447 ± 2.299
phase	10 km	102.617 ± 57.142	10.102 ± 4.294
phase	50 km	536.483 ± 286.159	34.717 ± 14.503
Doppler	5 km	8.660 ± 4.663	4.172 ± 2.165
Doppler	10 km	17.725 ± 9.496	6.253 ± 3.177
Doppler	50 km	86.869 ± 46.886	17.366 ± 8.281
phase+Doppler	5 km	27.887 ± 17.719	3.078 ± 1.519
phase+Doppler	10 km	56.232 ± 35.279	4.581 ± 2.360
phase+Doppler	50 km	286.742 ± 172.566	13.616 ± 6.611

Figure 2 shows how these gains unfold over time at the 10-km baseline. For the decimeter grade, the phase and phase+Doppler results converge rapidly, whereas the Doppler results approach the final accuracy more gradually. For the meter

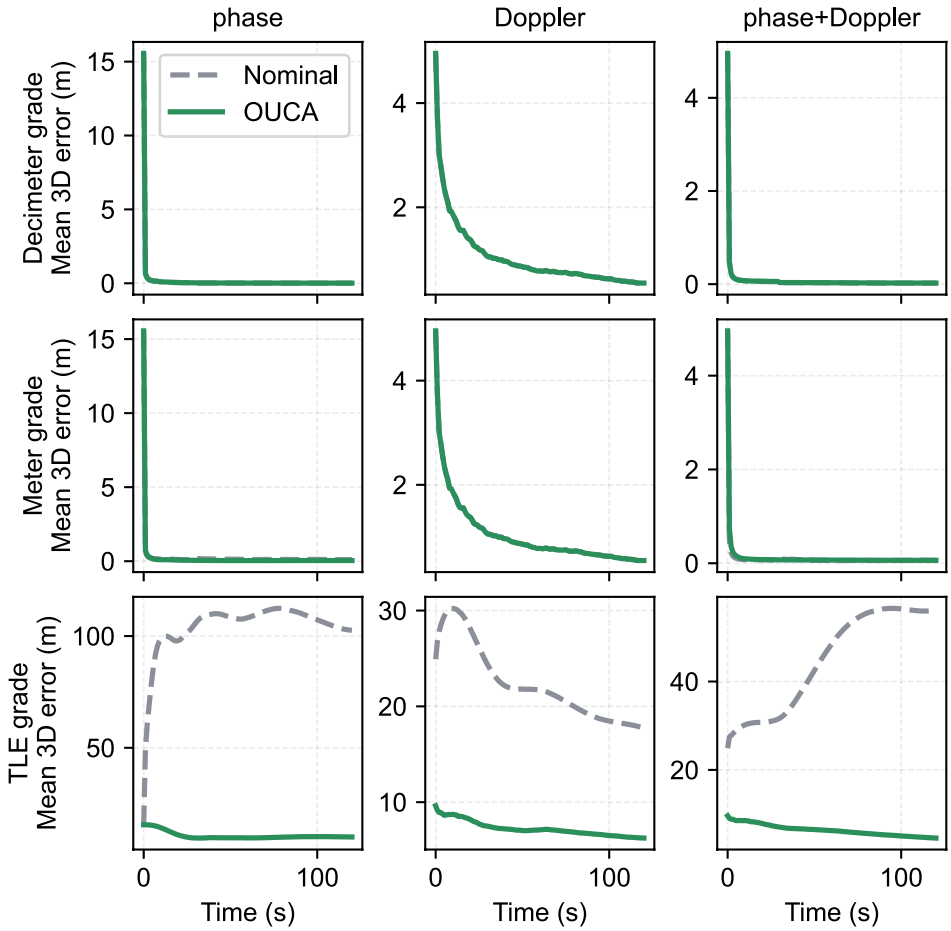

FIGURE 2 Epoch-by-epoch 3D error of nominal and OUCA results at the 10-km baseline Rows denote the decimeter, meter, and TLE grades, and columns denote the phase, Doppler, and phase+Doppler modes. OUCA leaves the precise-orbit behavior nearly unchanged, accelerates stabilization for the meter grade, and limits phase-driven drift in the TLE-grade phase+Doppler solution.

grade, OUCA accelerates the stabilization of the phase-based solutions. Under TLE-grade ephemeris, the nominal phase and phase+Doppler solutions diverge, whereas OUCA keeps all three modes bounded and convergent. The final OUCA errors are 10.102, 6.253, and 4.581 m for the phase, Doppler, and phase+Doppler modes, respectively. Taken together, Figures 1–2 show that OUCA not only reduces the final error, but also changes the transient behavior. OUCA accelerates convergence in moderate scenarios and turns divergence into stable convergence in the harsh TLE case.

4.3 | Comparison of Observation Modes Under OUCA

The next comparison applies the same covariance adaptation method to phase-only, Doppler-only, and phase+Doppler DD processing. Table 3 gives the mean final 3D errors and their standard deviations. The best single-observation mode changes from phase under high-precision orbit conditions to Doppler under TLE-grade orbit conditions. Under decimeter-grade ephemeris, the phase+Doppler mode retains centimeter-level accuracy. Under TLE-grade ephemeris, the phase+Doppler mode improves upon the best single mode at every baseline.

TABLE 3
Aggregated Final 3D Positioning Errors for the Three DD Observation Modes (Mean ± Standard Deviation; Errors Given in Meters)

Grade	Baseline	Phase (m)	Doppler (m)	Phase+Doppler (m)
dm	5 km	0.007 ± 0.005	0.596 ± 0.228	0.021 ± 0.016
dm	10 km	0.011 ± 0.007	0.545 ± 0.252	0.023 ± 0.017
dm	50 km	0.044 ± 0.030	0.584 ± 0.281	0.048 ± 0.027
m	5 km	0.048 ± 0.031	0.596 ± 0.228	0.050 ± 0.035
m	10 km	0.045 ± 0.028	0.547 ± 0.253	0.062 ± 0.044
m	50 km	0.210 ± 0.127	0.584 ± 0.286	0.097 ± 0.056
TLE	5 km	5.447 ± 2.299	4.172 ± 2.165	3.078 ± 1.519
TLE	10 km	10.102 ± 4.294	6.253 ± 3.177	4.581 ± 2.360
TLE	50 km	34.717 ± 14.503	17.366 ± 8.281	13.616 ± 6.611

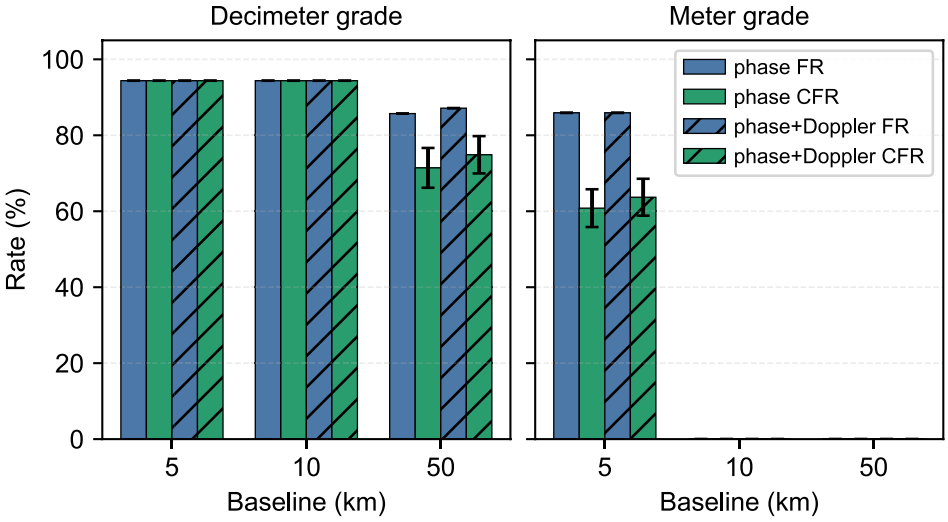

FIGURE 3 Final ambiguity-fixing statistics for the phase and phase+Doppler modes under OUCA for decimeter and meter orbit grades, with 100 tests per scenario
Bars show the mean final epoch FR and CFR, and error bars show the 95% confidence interval of the mean. TLE-grade cases are omitted because ambiguity fixing is disabled under kilometer-level orbit errors.

At 10 km, the error reaches 4.581 m, compared with 6.253 m for Doppler, an improvement of 26.7%.

Figure 3 compares the ambiguity resolution behavior of the phase and phase+Doppler DD modes under OUCA for the decimeter and meter orbit grades. The statistics are evaluated at the final epoch of each test. If N_{cand} is the number of DD ambiguity candidates available for PAR, N_{fix} is the number of candidates that are accepted and fixed, and N_{corr} is the number of fixed ambiguities that match the known simulated integer truth, then $\mathrm{FR} = N_{\mathrm{fix}}/N_{\mathrm{cand}} \times 100\%$ and $\mathrm{CFR} = N_{\mathrm{corr}}/N_{\mathrm{cand}} \times 100\%$.

The CFR is computed relative to the same candidate set as the FR and cannot exceed the FR. The bars show the mean over 100 tests, and the error bars show the 95% confidence interval of that mean. TLE-grade results are not shown because ambiguity fixing is disabled for the kilometer-level orbit error cases.

Under decimeter-grade ephemeris at 5 and 10 km, both the phase and phase+Doppler modes reach a 94.4% FR, and every fixed ambiguity is correct. At

50 km, their CFRs are 71.4% and 74.9%, respectively. Under meter-grade ephemeris at 5 km, both modes have an 85.9% FR, while their CFRs are 60.8% and 63.7%. Neither mode fixes ambiguities at 10 or 50 km. Thus, the phase+Doppler mode maintains or improves ambiguity-fixing performance relative to the phase mode under the tested high-precision orbit conditions.

4.4 | Sensitivity to Differencing Architecture: SD vs. DD

This experiment compares OUCA in SD and DD form under TLE-grade orbit conditions, where the contrast between the two architectures is strongest. The SD estimator retains receiver clock bias and drift states and remains as float, whereas DD removes these clock terms and supports ambiguity resolution. The comparison tests whether covariance adaptation remains effective when the differencing operator changes (Khalife & Kassas, 2023; Zhao et al., 2023).

Table 4 shows that the OUCA results remain stable in both architectures. The phase+Doppler SD solution reaches 2.998, 4.442, and 13.081 m at the 5-, 10-, and 50-km baselines, whereas the DD solution reaches 3.078, 4.581, and 13.616 m, respectively. The maximum difference is 0.535 m. In both architectures, the phase+Doppler solution improves upon the Doppler solution, the best single-observation mode, at every tested baseline. Across all modes, the SD and DD solutions remain close, with a maximum mean difference of 0.535 m. Because DD removes receiver clock bias and drift analytically, this remains the preferred architecture.

4.5 | Robustness to Covariance Mismatch

In practical applications, the scale and correlation structure of orbit uncertainty may not be known exactly. This section evaluates the performance of OUCA under four covariance mismatch scenarios. The first three scenarios introduce correlations in the truth model while the estimator assumes zero correlation. These correlations are between position and velocity, between the radial and transverse components, and between phase and Doppler noise. The fourth scenario changes the magnitude of the assumed orbit covariance while holding the injected error fixed. All tests use the TLE-grade DD phase+Doppler configuration at the 5-, 10-,

TABLE 4
Accuracy of Phase, Doppler, and Phase+Doppler Modes Under OUCA with SD and DD Processing in the TLE-Grade Scenarios (100-Test Mean ± Standard Deviation, Meters)

Mode	Baseline	SD OUCA (m)	DD OUCA (m)
phase	5 km	5.440 ± 2.296	5.447 ± 2.299
phase	10 km	10.084 ± 4.290	10.102 ± 4.294
phase	50 km	35.035 ± 14.712	34.717 ± 14.503
Doppler	5 km	4.052 ± 2.110	4.172 ± 2.165
Doppler	10 km	6.109 ± 3.088	6.253 ± 3.177
Doppler	50 km	16.946 ± 7.939	17.366 ± 8.281
phase+Doppler	5 km	2.998 ± 1.460	3.078 ± 1.519
phase+Doppler	10 km	4.442 ± 2.215	4.581 ± 2.360
phase+Doppler	50 km	13.081 ± 5.970	13.616 ± 6.611

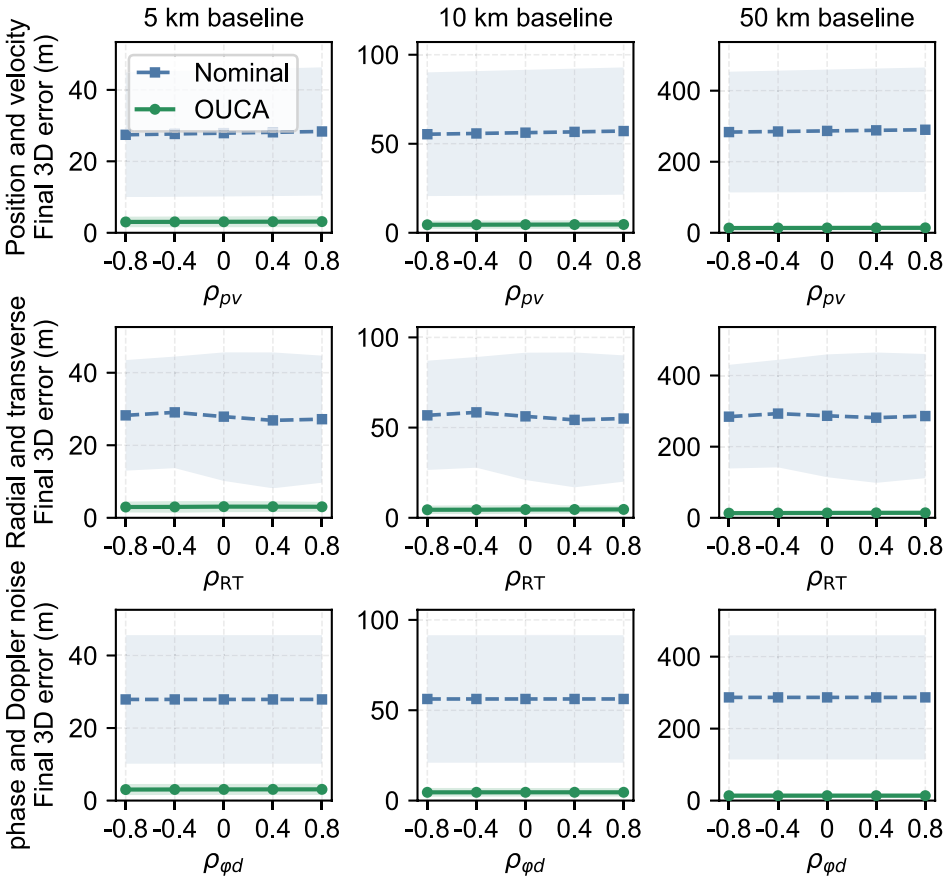

FIGURE 4 Final 3D error under position and velocity correlation ρ_{pv} (top), correlation between the radial and transverse components ρ_{RT} (middle), and phase and Doppler noise correlation $\rho_{\varphi d}$ (bottom)
The truth model carries the indicated correlation while the estimator assumes zero correlation. Columns denote the baseline length. Curves and shaded bands show the mean and standard deviation over 100 tests.

and 50-km baselines over the same 100 tests as the main matrix. The reference setting is $k=1$ for the magnitude test and $\rho_{pv}=0$, $\rho_{RT}=0$, or $\rho_{\varphi d}=0$ for the corresponding correlation test. Each reference setting reproduces the main matrix results of 3.078, 4.581, and 13.616 m for OUCA and 27.887, 56.232, and 286.742 m for the nominal case. Only one parameter is varied between paired tests.

In Figure 4, the three true correlations are varied from −0.8 to 0.8, while the estimator assumes zero correlation. The largest OUCA value changes from the zero-correlation reference are 3.3%, 2.8%, and 4.3% at the 5-, 10-, and 50-km baselines, respectively. The OUCA value remains within 2.977–3.130, 4.454–4.658, and 13.027–14.004 m, whereas the nominal result ranges from 26.86 to 292.92 m. OUCA therefore retains its improvement when the true correlation structure differs from the assumed model.

In Figure 5, the assumed RTN standard deviations are multiplied by $k \in \{0.5, 0.75, 1, 1.5, 2\}$ while the injected orbit error is held fixed. For a factor of two in the mismatch, the largest OUCA errors are 3.791, 6.123, and 16.519 m at the three baselines, substantially below the corresponding nominal errors of 27.887, 56.232, and 286.742 m. Underestimation is more detrimental because it gives excessive weight to phase observations affected by orbit error, whereas overestimation produces conservative weighting. Therefore, OUCA is more sensitive to covariance magnitude than to the omitted correlations and remains substantially more

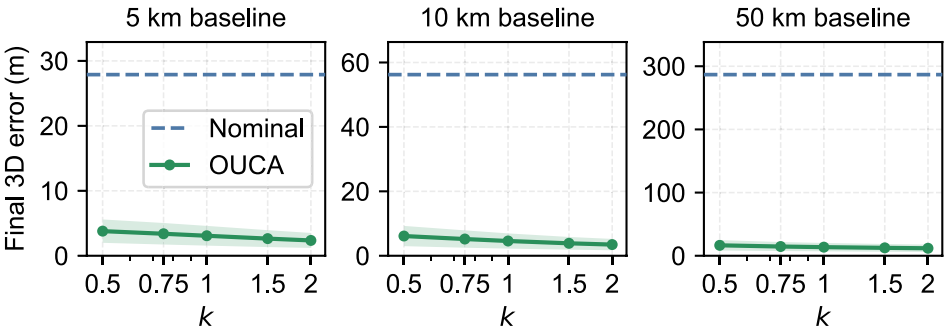

FIGURE 5 Final 3D error against the model uncertainty scale k
The injected orbit error is fixed, while the assumed RTN standard deviations and covariance are multiplied by k and k^2, respectively. The matched setting is $k = 1$. Curves and shaded bands show the mean and standard deviation over 100 tests.

accurate than the nominal approach. Operational use requires orbit uncertainty statistics obtained from the product provider, historical product assessment, or an external orbit-monitoring service (Huang et al., 2026; Khairallah & Kassas, 2024).

5 | CONCLUSION

This work leads to two main conclusions. First, OUCA is a covariance adaptation layer that benefits all three observation modes. By mapping prior orbit uncertainty into the observation covariance, OUCA aligns measurement weighting with the propagated uncertainty. For the phase-only mode, OUCA reduces the TLE errors from 102.617 to 10.102 m at the 10-km baseline and from 536.483 to 34.717 m at 50 km. For the Doppler-only mode, the corresponding errors decrease from 17.725 to 6.253 m and from 86.869 to 17.366 m. Covariance mismatch tests further show that OUCA retains a substantial improvement under errors in the assumed covariance magnitude and unmodeled position–velocity, RTN component, and phase–Doppler noise correlations.

Second, once OUCA is applied, the phase+Doppler mode provides an effective joint solution across different orbit-quality conditions. Under high-precision orbit conditions, this mode retains centimeter-level positioning accuracy and maintains or improves ambiguity-fixing performance compared with the phase mode. Under TLE-grade orbit conditions, the phase+Doppler mode improves positioning accuracy compared with the Doppler mode at every tested baseline. At 10 km, the phase+Doppler mode reaches 4.581 m, compared with 6.253 m for the Doppler mode, an improvement of 26.7%.

The mismatch experiments show that OUCA is relatively insensitive to unmodeled correlations but more sensitive to the scale of the assumed orbit covariance. An overly loose specification leads to conservative weighting. An overly optimistic specification may leave orbit-induced bias insufficiently represented in the observation covariance. Future work should calibrate RTN covariance models as functions of TLE age and orbital phase using successive TLEs and operator-provided ephemerides. Thus, sensitivity to covariance mis-specification, including practical TLE-quality variability, should be examined in future operational studies. From a computational perspective, OUCA introduces per-epoch RTN-to-ECEF rotations and per-satellite covariance projections. These are algebraic covariance propagation steps, but their scaling behavior for real-time processing and very large LEO constellations should also be assessed in future work.

ACKNOWLEDGMENTS

This work was supported by the Australian Research Council through Discovery Project DP240101710.

CONFLICT OF INTEREST

The authors declare no potential conflicts of interest with respect to the research, authorship, or publication of this article.

REFERENCES

Allahvirdi-Zadeh, A., El-Mowafy, A., & Wang, K. (2025). Doppler positioning using multi-constellation LEO satellite broadband signals as signals of opportunity. *NAVIGATION*, *72*(2). https://doi.org/10.33012/navi.691

Allahvirdi-Zadeh, A., El-Mowafy, A., & Wang, K. (2026). Network-based precise orbit determination of broadband LEO satellites using Doppler-shift measurements. *GPS Solutions*, *30*(1), 16. https://doi.org/10.1007/s10291-025-01963-0

Baron, A., Gurfil, P., & Rotstein, H. (2024). Implementation and accuracy of Doppler navigation with LEO satellites. *NAVIGATION*, *71*(2). https://doi.org/10.33012/navi.649

Del Portillo, I., Cameron, B. G., & Crawley, E. F. (2019). A technical comparison of three low earth orbit satellite constellation systems to provide global broadband. *Acta Astronautica*, *159*, 123–135. https://doi.org/10.1016/j.actaastro.2019.03.040

Diouf, C., Janssen, G. J. M., Dun, H., Kazaz, T., & Tiberius, C. C. J. M. (2021). A USRP-based testbed for wideband ranging and positioning signal acquisition. *IEEE Transactions on Instrumentation and Measurement*, *70*, 1–15. https://doi.org/10.1109/TIM.2021.3065449

Dun, H., Tiberius, C. C. J. M., & Janssen, G. J. M. (2020). Positioning in a multipath channel using OFDM signals with carrier phase tracking. *IEEE Access*, *8*, 13011–13028. https://doi.org/10.1109/ACCESS.2020.2966070

Elgamoudi, A., Benzerrouk, H., Elango, G. A., & Landry, R. (2020). Gauss hermite h_∞ filter for UAV tracking using LEO satellites TDOA/FDOA measurement—part i. *IEEE Access*, *8*, 201428–201440. https://doi.org/10.1109/ACCESS.2020.3032825

El-Mowafy, A., Wang, K., Li, Y., & Allahvirdi-Zadeh, A. (2023). The impact of orbital and clock errors on positioning from LEO constellations and proposed orbital solutions. *The International Archives of the Photogrammetry, Remote Sensing and Spatial Information Sciences*, *XLVIII-1/W2-2023*, 1111–1117. https://doi.org/10.5194/isprs-archives-XLVIII-1-W2-2023-1111-2023

Farhangian, F., & Landry, R. (2020). Multi-constellation software-defined receiver for Doppler positioning with LEO satellites. *Sensors*, *20*(20), 5866. https://doi.org/10.3390/s20205866

Garcia, J., Sundberg, S., & Brunstrom, A. (2024, January). Fine-grained Starlink throughput variation examined with state-transition modeling. In *2024 19th Wireless On-Demand Network Systems and Services Conference (WONS)* (pp. 69–76). https://doi.org/10.23919/WONS60642.2024.10449629

Gholami, M. R., Gezici, S., & Strom, E. G. (2013). TDOA based positioning in the presence of unknown clock skew. *IEEE Transactions on Communications*, *61*(6), 2522–2534. https://doi.org/10.1109/TCOMM.2013.032013.120381

Huang, J., Wei, H., & Zou, X. (2026). Accuracy assessment and comparative analysis of operator ephemeris and TLE data for the Starlink constellation. *Geomatics and Information Science of Wuhan University*. https://doi.org/10.13203/j.whugis20260018

Humphreys, T. E., Iannucci, P. A., Komodromos, Z. M., & Graff, A. M. (2023). Signal structure of the Starlink ku-band downlink. *IEEE Transactions on Aerospace and Electronic Systems*, *59*(5), 6016–6030. https://doi.org/10.1109/TAES.2023.3268610

Iannucci, P. A., & Humphreys, T. E. (2024). Fused low-earth-orbit GNSS. *IEEE Transactions on Aerospace and Electronic Systems*, *60*(4), 3730–3749. https://doi.org/10.1109/TAES.2022.3180000

Jiang, M., Qin, H., Zhao, C., & Sun, G. (2021). LEO Doppler-aided GNSS position estimation. *GPS Solutions*, *26*(1), 31. https://doi.org/10.1007/s10291-021-01210-2

Kazaz, T., Janssen, G. J. M., Romme, J., & der Veen, A.-J. (2022). Delay estimation for ranging and localization using multiband channel state information. *IEEE Transactions on Wireless Communications*, *21*(4), 2591–2607. https://doi.org/10.1109/TWC.2021.3113771

Khairallah, N., & Kassas, Z. M. (2024). Ephemeris tracking and error propagation analysis of LEO satellites with application to opportunistic navigation. *IEEE Transactions on Aerospace and Electronic Systems*, *60*(2), 1242–1259. https://doi.org/10.1109/TAES.2023.3325797

Khalife, J., & Kassas, Z. Z. M. (2023). Performance-driven design of carrier phase differential navigation frameworks with megaconstellation LEO satellites. *IEEE Transactions on Aerospace and Electronic Systems*, *59*(3), 2947–2966. https://doi.org/10.1109/TAES.2023.3234521

Khalife, J., Neinavaie, M., & Kassas, Z. M. (2020, May). Navigation with differential carrier phase measurements from megaconstellation LEO satellites. In *2020 IEEE/ION Position,*

Location and Navigation Symposium (PLANS) (pp. 1393–1404). https://doi.org/10.1109/PLANS46316.2020.9110199

Khalife, J., Neinavaie, M., & Kassas, Z. Z. (2022). The first carrier phase tracking and positioning results with Starlink LEO satellite signals. *IEEE Transactions on Aerospace and Electronic Systems*, *58*(2), 1487–1491. https://doi.org/10.1109/TAES.2021.3113880

Kozhaya, S., Saroufim, J., & Kassas, Z. M. (2025). Unveiling Starlink for PNT. *NAVIGATION 72*(1), navi.685. https://doi.org/10.33012/navi.685

Leng, M., Quitin, F., Tay, W. P., Cheng, C., Gulam Razul, S., & Samson See, C. M. (2016). Anchor-aided joint localization and synchronization using soop: Theory and experiments. *IEEE Transactions on Wireless Communications*, *15*(11), 7670–7685. https://doi.org/10.1109/TWC.2016.2606099

Leng, M., Tay, W. P., See, C. M. S., Gulam Razul, S., & Win, M. Z. (2014). Modified CRLB for cooperative geolocation of two devices using signals of opportunity. *IEEE Transactions on Wireless Communications*, *13*(7), 3636–3649. https://doi.org/10.1109/TWC.2014.2314096

Levit, C., & Marshall, W. (2011). Improved orbit predictions using two-line elements. *Advances in Space Research*, *47*(7), 1107–1115. https://doi.org/10.1016/j.asr.2010.10.017

Li, Q., Yao, W., Tu, R., Du, Y., & Liu, M. (2023). Performance assessment of multi-GNSS PPP ambiguity resolution with LEO-augmentation. *Remote Sensing*, *15*(12), 2958. https://doi.org/10.3390/rs15122958

Li, X., Li, X., Ma, F., Yuan, Y., Zhang, K., Zhou, F., & Zhang, X. (2019). Improved PPP ambiguity resolution with the assistance of multiple LEO constellations and signals. *Remote Sensing*, *11*(4), 408. https://doi.org/10.3390/rs11040408

Liu, A.-r., Xiong, Y.-q., Hui, J.-j., Xu, X.-l., & Gong, J. (2025). Research on Starlink ephemeris published by SpaceX. *Chinese Astronomy and Astrophysics*, *49*(1), 193–218. https://doi.org/10.1016/j.chinastron.2025.03.005

Liu, P., Qin, H., Lu, J., Liu, R., Guan, Y. L., Ling, K. V., & Yuen, C. (2025). Positioning with LEO satellites as signals of opportunity (SoOP): A survey. *IEEE Transactions on Instrumentation and Measurement*, *74*, 1–21. https://doi.org/10.1109/TIM.2025.3645906

Niell, A. E. (1996). Global mapping functions for the atmosphere delay at radio wavelengths. *Journal of Geophysical Research: Solid Earth*, *101*(B2), 3227–3246. https://doi.org/10.1029/95JB03048

Pan, C., Li, Z., Gao, J., & Li, F. (2021). A variational Bayesian-based robust adaptive filtering for precise point positioning using undifferenced and uncombined observations. *Advances in Space Research*, *67*(6), 1859–1869. https://doi.org/10.1016/j.asr.2020.12.022

Psiaki, M. L. (2021). Navigation using carrier Doppler shift from a LEO constellation: Transit on steroids. *NAVIGATION*, *68*(3), 621–641. https://doi.org/10.1002/navi.438

Shi, C., Zhang, Y., & Li, Z. (2023). Revisiting Doppler positioning performance with LEO satellites. *GPS Solutions*, *27*(3), 1–16. https://doi.org/10.1007/s10291-023-01466-w

Vallado, D. A., Crawford, P., Hujsak, R., & Kelso, T. S. (2006, August). Revisiting spacetrack report #3. In *AIAA/AAS Astrodynamics Specialist Conference and Exhibit* (pp. 1–29). https://doi.org/10.2514/6.2006-6753

Wang, K., El-Mowafy, A., & Rizos, C. (2022). Integrity monitoring for precise orbit determination of LEO satellites. *GPS Solutions*, *26*(1), 32. https://doi.org/10.1007/s10291-021-01200-4

Yang, S., Khodabandeh, A., Zaminpardaz, S., & Teunissen, P. J. G. (2025). Ambiguity-resolved short-baseline positioning performance of LEO frequency-varying carrier phase signals: A feasibility study. *Journal of Geodesy*, *99*(2), 17. https://doi.org/10.1007/s00190-025-01942-w

Yang, Y., He, H., & Xu, G. (2001). Adaptively robust filtering for kinematic geodetic positioning. *Journal of Geodesy*, *75*, 109–116. https://doi.org/10.1007/s001900000157

Zhao, C., Qin, H., Wu, N., & Wang, D. (2023). Analysis of baseline impact on differential Doppler positioning and performance improvement method for LEO opportunistic navigation. *IEEE Transactions on Instrumentation and Measurement*, *72*, 1–10. https://doi.org/10.1109/TIM.2023.3235456

How to cite this article: Yu, Y., El-Mowafy, A., & Allahvirdi-Zadeh, A. (2026). Orbit uncertainty covariance adaptation for LEO phase and Doppler differential positioning. *NAVIGATION*, *73*. https://doi.org/10.33012/navi.793